A NOVEL TOTAL LAGRANGIAN SMOOTHED PARTICLE HYDRODYNAMICS APPROACH FOR MODELING DAMAGE IN ELASTIC SOLIDS AND DEFORMATION OF COMPOSITE STRUCTURES

by
GOKTUG KILIC

Submitted to the Graduate School of Engineering and Natural Sciences
in partial fulfilment of
the requirements for the degree of Doctor of Philosophy

Sabanci University
July 2025

A NOVEL TOTAL LAGRANGIAN SMOOTHED PARTICLE HYDRODYNAMICS APPROACH FOR MODELING DAMAGE IN ELASTIC SOLIDS AND DEFORMATION OF COMPOSITE STRUCTURES

Approved by:

Prof. MEHMET YILDIZ .....
(Dissertation Supervisor)

Prof. BURC MISIRLIOGLU .....

Assoc. Prof. HATICE SINEM SAS CAYCI .....

Prof. HALIT SULEYMAN TURKMEN .....

Asst. Prof. POYRAZ AYDINER .....

Date of Approval: July 16, 2025

ABSTRACT

A NOVEL TOTAL LAGRANGIAN SMOOTHED PARTICLE HYDRODYNAMICS APPROACH FOR MODELING DAMAGE IN ELASTIC SOLIDS AND DEFORMATION OF COMPOSITE STRUCTURES

GOKTUG KILIC

MATERIALS SCIENCE AND NANOENGINEERING Ph.D DISSERTATION, JULY 2025

Dissertation Supervisor: Prof. MEHMET YILDIZ

Keywords: meshless methods, crack propagation, smoothed particle hydrodynamics, composite

This thesis comprehensively investigates Total Lagrangian Smoothed Particle Hydrodynamics (TLSPH) for modeling complex failure and deformation in solid mechanics by focusing on dynamic brittle fracture and quasi-static deformation of laminated composite structures. In the first part, a novel TLSPH framework for crack initiation and propagation is developed. Overcoming mesh-based method limitations such as FEM's mesh dependence and remeshing, this mesh-free model solves the strong form of linear momentum equations using a fully Lagrangian particle formulation. Damage is modeled via a stretch-based criterion, with particle interactions deactivated at critical stretch. Numerical instabilities are mitigated by enhanced diffusion and velocity filtering in damaged zones. Validated against 2D and 3D benchmarks (e.g., Kalthoff-Winkler experiment, dynamic crack branching), the framework demonstrates accuracy, robustness, and captures complex crack paths without remeshing. The second part extends TLSPH to model quasi-static deformation of laminated composite beams and plates. This is the first comprehensive 3D TLSPH application to orthotropic composite laminates, discretizing each ply through thickness using corrected kernel gradients. Laminae are modeled as orthotropic continua, with global stiffness via exact tensor transformations. Hourglass control and artificial viscosity ensure stabilization. Benchmark studies (bi-layer carbon/epoxy cantilever beams, clamped square plate) confirm accuracy against

high-fidelity FEM by capturing linear through-thickness in-plane displacements and bending-stretching coupling. A parametric study of hourglass coefficients further explores damping-accuracy trade-offs. Overall, this thesis establishes TLSPH as a versatile, robust, mesh-independent tool for simulating deformation and fracture in isotropic and anisotropic media, bridging a key gap by unifying fracture mechanics and composite structural analysis within a single framework.

ÖZET

ELASTIK KATILARDA HASAR VE KOMPOZIT YAPILARIN DEFORMASYONUNU MODELLEMEK IÇIN YENI BIR TOPLAM LAGRANGE INTERPOLASYONLU PARÇACIK HIDRODINAMIGI YAKLASIMI

GOKTUG KILIC

MALZEME BILIMI VE NANOMUHENDISLIK DOKTORA TEZI, TEMMUZ 2025

Tez Danismani: Prof. Dr. MEHMET YILDIZ

Anahtar Kelimeler: agsiz yöntemler, çatlak ilerlemesi, interpolasyonlu parçacik hidrodinamigi, kompozit

Bu tez, kati mekaniginde Toplam Interpolasyonlu Düzgünlestirilmis Parçacik Hidrodinamigi (TLSPH) kullanimina odaklanir; dinamik gevrek kirilma ve lamine kompozitlerin yari-statik deformasyonunu inceler. Ilk bölümde, çatlak baslatma ve ilerlemesi için agsiz bir TLSPH çerçevesi gelistirilmistir. Sonlu Elemanlar Yöntemi (FEM)'in ag bagimliligi ve yeniden ag olusturma sorununu asarak, lineer momentum denklemlerini Lagrangian formülasyonuyla çözer. Hasar, kritik gerilime dayali bir kriterle modellenir; sayisal kararsizliklar difüzyon ve hiz filtrelemesiyle azaltilir. Bu method, iki ve üç boyutlu kiyaslamalarla (Kalthoff-Winkler ve dinamik çatlak çatallanmasi deneyleri) dogrulanmistir ve bu methodun yeniden ag olusturma gerektirmeden karmasik çatlak ilerlemesini yakalama yetenegi, dogrulugu ve saglamligi gösterilmistir. Ikinci bölümde, TLSPH lamine kompozit kiris ve plakalarin yaristatik deformasyonunu modellemek üzere genisletilmistir. Bu, ortotropik laminatlarda 3D TLSPH'nin ilk kapsamli uygulamasidir. Yöntem, her katmani kalinlik boyunca ayriklastirir; denklemleri düzeltilmis kernel gradyanlari kullanarak çözer. Stabilizasyon, kum saati kontrolü ve yapay viskozite ile saglanmistir. Kiyaslama çalismalari (karbon/epoksi konsol kirisler, kare plaka) FEM çözümlerine karsi dogrulugu teyit eder; düzlem içi yer degistirmelerin kalinlik boyunca dogrusal degisimini ve asimetrik laminatlardaki bükülme-uzama birlesimini yakalar. Kum saati

katsayisi çalismasi, sönümleme ve dogruluk arasindaki ödünlesimleri inceler. Genel olarak, tez TLSPH'yi izotropik ve anizotropik ortamda kirilma mekanigi ile kompozit yapisal analizini birlestiren, saglam, agsiz, çok yönlü bir araç olarak sunarak literatürdeki boslugu doldurur.

ACKNOWLEDGEMENTS

I would first like to express my sincere gratitude to my thesis advisor, Prof. Dr. Mehmet Yildiz, for his academic guidance and for providing me the opportunity to pursue this research under his supervision. I am especially grateful to Dr. Deniz Can Kolukisa, whose support and mentorship were instrumental throughout this journey. His expertise in Smoothed Particle Hydrodynamics, combined with his remarkable patience and willingness to answer every question I had played a crucial role in my development and the completion of this work. I also wish to thank Dr. Poyraz Aydiner for his contributions and involvement in the second part of my thesis.

I am deeply thankful to Sabanci University for its outstanding academic and institutional support throughout my PhD journey. The university provided not only a highly supportive research environment but also an excellent campus life. In every aspect, Sabanc University has proven to be one of the best institutions in Türkiye for pursuing doctoral studies.

I am also grateful to the Sabanc University - Integrated Manufacturing Technologies Research and Application Center (SU-IMC), established under the leadership of my advisor. SU-IMC provided the computational infrastructure necessary for my work, including access to a high-performance computing cluster for running large-scale simulations. Beyond its technical resources, it fostered a warm environment where I had the chance to meet wonderful fellow graduate students who made this journey far more enjoyable.

I gratefully acknowledge the financial support provided by the Scientific and Technological Research Council of Türkiye (TUBITAK) under the 2244 - Industry PhD Program (Project No. 118C049), carried out in collaboration between Sabanci University and ROKETSAN. I also thank ROKETSAN for their contribution to my scholarship and for offering the opportunity to continue my professional development within their organization. The support of both institutions has been instrumental in enabling the successful completion of this research.

I am especially thankful to my beloved family for their unconditional love and lifelong support. I am the son of Ismail Kilic, a retired police officer, and Fatma Kilic, a devoted homemaker. Although they did not have the opportunity to pursue higher education themselves, they have always stood by me and made every possible sacrifice to support my academic journey. I would not be who I am today without their

unwavering love and encouragement.

I am also profoundly grateful to my older sister, Tugba Kilic, who has always been like a second mother to me. She not only helped raise me alongside my parents but also made me an uncle at the age of six a role that has filled my life with joy through her two wonderful sons and two lovely daughters. Because of her, I have had the privilege of growing up with younger siblings in spirit, even as the youngest child in our family. I also thank my older brother, Ahmet Kilic, for his support and presence throughout my life. The love, strength, and encouragement I have received from all of them have sustained me through every challenge of this long journey.

I am also grateful to all of my friends, but especially to my dear friend Idil Ertem, who made my first years at Sabanci University truly unforgettable. She brought joy and friendship into my daily life, and together we created memories across the campus that we still laugh aboutand likely always will. She is, without doubt, the most valuable person this university has brought into my life.

Finally, I wish to express my sincere thanks to Burak Kilickaya, whose constant support, understanding, and presence have been a great source of strength and motivation throughout this journey. His kindness and encouragement have made even the most challenging times more bearable.

To my mother, Fatma Kilic, the strongest woman I have ever known. Your resilience, love, and sacrifices have carried our family through everything.

To my father, Ismail Kilic. Time has shown me the depth of your love and pride in me. Thank you for your quiet strength and your support.

TABLE OF CONTENTS

LIST OF TABLES

LIST OF FIGURES

1. INTRODUCTION

Computational modeling and simulation have become essential tools in engineering because it enables the prediction of complex physical phenomena where analytical solutions are intractable or experiments are costly. In solid mechanics, given the critical importance of understanding material failure mechanisms, optimizing structural designs, and ensuring structural integrity, computational modeling and simulation are highly favored methodologies. Finite Element Method (FEM) has been an excellent mathematical approach due to its versatility, standardized frameworks and widespread integration within commercial software platforms. While FEM excels for problems with moderate deformations and smooth material behavior, its inherent mesh-dependent formulation presents limitations in accurately simulating complex phenomena such as large deformations, dynamic fracture, crack propagation, and heterogeneous media (Belytschko & Black, 1999; de Borst, Crisfield, Remmers & Verhoosel, 2012; Rabczuk, 2013). The necessity of iterative remeshing in FEM - which is essential for modeling dynamic crack propagation and prevent mesh distortion during large deformation - results in high computational costs that limit its practical implementation. The eXtended Finite Element Method (XFEM) (Moës & Belytschko, 2002; Sukumar, Moës, Moran & Belytschko, 2000) eliminates some issues but the mesh-dependency of the crack path has not been fully eliminated. Furthermore, both FEM and XFEM face inherent challenges in problems involving large deformations (e.g., ballistic impacts, composite crushing), where mesh distortion introduces numerical instabilities. These persistent limitations have driven significant interest in meshless methods.

1.1 Meshless Methods

Recent advances in computational mechanics have increasingly favored meshless methods due to their inherent ability to overcome the mesh-related constraints of FEM and XFEM (Liew, Zhao & Ferreira, 2011) by eliminating predefined element connectivity. By approximating field variables using only nodal points without mesh constraints, these approaches inherently avoid remeshing requirements and mesh distortion issues. This fundamental characteristic provides greater flexibility for modeling discontinuities and large deformations while simplifying the simulation of complex phenomena where traditional mesh-based methods struggle. This section provides a brief literature review on some of the meshless methods and their applications in crack propagation and composite modeling.

The Element-Free Galerkin Method (EFGM) (Belytschko, Lu & Gu, 1994) which is based on Moving Least Squares (MLS) interpolation (Shepard, 1968), approximates field variables using scattered nodes with polynomial functions and variable coefficients. While EFGM eliminates element connectivity, it retains dependence on background meshes for numerical integration. Belytschko et al. (Belytschko, Lu & Gu, 1995; Belytschko & Tabbara, 1996) used EFGM for crack propagation problem their work in which the crack surface is explicitly modeled. Rabczuk and Belytschko (Rabczuk & Belytschko, 2004,0) later proposed the cracking particle method. This method simulates a crack in the body with discrete cracks on t2he particles, eliminating explicit crack surface representation. The accuracy is maintained by additional functions for the displacement field around the crack. The need for utilizing extra functions is removed in particle splitting method (Rabczuk, Zi, Bordas & Nguyen-Xuan, 2010) in which a particle is split and forms two new particles upon crack initiation. On the other hand, EFGM is also implemented for composite structures. The buckling behavior of both the isotropic and laminated composite plates is investigated by Liu et al. (Liu, Chen & Reddy, 2002) by employing the weak form of the governing equations. They reported that the dimension of the EFGM eigenvalue problem is smaller compared to FEM. In Zhou and Song's study (Zhou & Song, 2019), Strain-Rotation decomposition theorem is used with EFGM to analyze the bending behavior of carbon nanotube reinforced composite plates by stressing the limitations of finite deformation theory in nonlinear scenarios. In (Ghorashi, Mohammadi & Sabbagh-Yazdi, 2011; Pan, Li, Luo & Zhu, 2022), fracture in composite material is simulated via EFGM with the weak formulations.

The Radial Point Interpolation Method (RPIM) (Wang & Liu, 2002) is an another meshless technique. In this method, the shape functions are constructed based on radial basis functions and a combination of radial and polynomial functions for the interpolation of physical variables are utilized. This dual function approach can result in a higher computational cost. Gu et al. (Gu, Wang, Zhang & Feng,

2011) developed enriched RPIM method where they enhance the standard RPIM interpolation with trigonometric basis functions for determining the crack tip stress. Compared to conventional RBF, e-RPIM offers improved accuracy. In Zhuang et al.'s study(Zhuang, Cai & Augarde, 2014), meshless sub-region RPIM is developed. Their methodology employs Williams series expansions as trial functions within crack tip region, while utilizing conventional RPIM for the regions far away the crack tip. Thus, they enabled accurate determination of crack tip stress fields with a sparse nodal discretization around the crack tip. Ramalho et al. (Ramalho, Belinha & Campilho, 2019) combined RPIM and Natural Neighbor RPIM for the different integration schemes of each. NNRPIM distinguishes itself by constructing background integration points solely from the spatial coordinates of the nodes. While RPIM is utilized for numerical solution of partial differential equations, NNRPIM background mesh structure is formed for the crack tip regions. This allows for efficient crack tip stress analysis with a reduced nodal density in the vicinity of the crack. RPIM has also been applied to composite structures. Saitta et al. (Saitta, Luciano, Vescovini, Fantuzzi & Fabbrocino, 2022) integrated RPIM into nonlocal strain gradient theory for the dynamic analysis of cross-ply composite nanoplates by incorporating a nonlocal parameter to account for nano effects. Similarly, Rodrigues et al. (Rodrigues, Belinha, Dinis & Jorge, 2021; Rodrigues, Belinha & Natal Jorge, 2021) employed RPIM to conduct static bending analysis of symmetric and anti-symmetric laminates using various higher-order shear deformation theories. Both RPIM and EFGM utilize a background mesh structure for the integration of the field variables.

Peridynamics stands as a prominent meshless method for the simulation of discontinuities, attributed to its formulation based on integro-differential governing equations (Silling, 2000) and material discontinuities are inherently incorporated within the constitutive formulation (Madenci & Oterkus, 2013). Peridynamics establishes inter-particle interactions through the concept of bonds, the characteristics of which are linked to the material's energy release rate. Exceedance of a critical strain threshold of a bond represents fracture initiation an/or propagation. While peridynamics theory provides a robust framework for simulating discontinuities, the development of novel material models necessitates rigorous mathematical derivation or reformulation. Ghajari et al. (Ghajari, Iannucci & Curtis, 2014) and Guo et al. (Guo, Tian & Tang, 2024) introduced composite peridynamics models wherein the elastic modulus of a bond connecting two particles is defined as a function of their relative fiber orientations, with the specific functional form differing between the two studies. Mehrmashhadi et al. (Mehrmashhadi, Chen, Zhao & Bobaru, 2019) developed fully-homogenized and intermediately-homogenized peridynamics models

to analyze and compare intraply quasi-static fracture in fiber-reinforced composite structures. For the intermediately-homogenized model, they employed a stochastic methodology to differentiate the properties of fiber-fiber, matrix-matrix, and fiber-matrix bonds.

The meshless methods discussed above have demonstrated significant potential for modeling both crack propagation and composite behavior, each offering distinct advantages: EFGMs accuracy in crack-tip modeling, RPIMs flexibility in stress field approximation, and Peridynamics inherent treatment of discontinuities. However, these approaches share common limitations, including reliance on background integration meshes, high computational costs, and/or complex constitutive formulations. These constraints motivate the exploration of Smoothed Particle Hydrodynamics (SPH) as an alternative. In the following section, SPH is introduced with an extensive literature review on its applications in crack propagation and composite structures.

1.2 Smoothed Particle Hydrodynamics

SPH was first introduced in 1977 by Gingold and Monaghan (Gingold & Monaghan, 1977) and Lucy (Lucy, 1977) for astrophysical problems and is considered as one of the earliest meshless methods. In SPH, the computational domain is discretized into particles, each possessing a neighborhood defined by a characteristic smoothing length. Field variables are interpolated non-locally through a smoothing kernel function based on neighboring particles. SPH's theoretical simplicity and inherent ability to handle complex interfaces and moving boundaries have made it a valuable tool for particularly in fluid dynamics (He, Tofighi, Yildiz, Lei & Suleman, 2017; Rahimi, Koluksa, Yildiz, Ozbulut & Kefal, 2022; Rahmat & Yildiz, 2018). SPH has increasingly been adopted in solid mechanics for its inherent ability to adress mesh-related challenges, including remeshing requirements and stress singularities near discontinuities. This capability has made it particularly valuable for simulating large deformations (Jun Lin, Naceur, Daniel & Laksimi, 2015; Lin, Naceur, Coutellier & Laksimi, 2014; Zhang, Ming & Cao, 2014), hypervelocity impacts (Cherniaev & Telichev, 2015; Giannaros, Kotzakolios, Kostopoulos & Campoli, 2019; Libersky, Petschek, Carney, Hipp & Allahdadi, 1993), and fracture propagationscenarios where traditional mesh-based methods struggle.

Despite its advantages, SPH remains susceptible to two major numerical instabilities: tensile instability and rank deficiency. The tensile instability phenomenon, first identified by Swegle (Swegle, Hicks & Attaway, 1995), manifests when tensile stresses cause normally repulsive inter-particle forces to become attractive, leading to artificial particle clustering. Belytschko et al. (Belytschko, Guo, Kam Liu & Ping Xiao, 2000) attributed this instability to the fundamental conflict between the Eulerian nature of kernel approximation and the Lagrangian motion of particles. This instability was addressed by Belytschko et al. (Belytschko, Guo, Kam Liu & Ping Xiao, 2000) by developing the Total Lagrangian SPH (TL-SPH) method, which performs kernel approximation in the undeformed reference configuration. However, this approach can become problematic under extreme deformations due to significant support domain distortion. This limitation has motivated alternative approaches such as the updated Lagrangian scheme proposed by Rabczuk and Belytschko (Rabczuk & Belytschko, 2007), where the kernel function is periodically updated during the simulation. Rank deficiency presents another significant challenge in SPH simulations, as extensively discussed by Dyka et al. (Dyka, Randles & Ingel, 1997). This issue primarily stems from SPH's inherent nodal integration approach, which can violate the zeroth and first-order consistency conditions of the kernel function. As a result of this violation, spurious energy modes and incomplete displacement field representations are generated. Several mitigation strategies have been developed, including the use of additional integration points (Dyka, Randles & Ingel, 1997; Randles & Libersky, 1996), stabilized conforming nodal integration methods (Chen, Wu, Yoon & You, 2001), and hourglass stabilization techniques. Ganzenmüller (Ganzenmüller, 2015) specifically addressed the computational expense of increased integration points in Lagrangian SPH by developing an alternative stabilization approach that introduces an hourglass force term into the momentum equation to suppress resulting hourglass modes. Furthermore, kernel gradient correction techniques have proven effective in satisfying first-order completeness conditions and improving solution accuracy.

Several studies in the literature have employed SPH for crack modeling applications. Benz and Asphaug (Benz & Asphaug, 1995) established an SPH framework for brittle fracture and fragmentation using explicit equations to predict crack evolution. Their method requires a probabilistic definition of initial material flaws coupled with a complex failure criterion that presents implementation challenges. A pseudo-spring based SPH was proposed by Chakraborty and Shaw (Chakraborty & Shaw, 2013) for modeling an impact scenario. In their study, damage accumulation progressively reduces spring forces between adjacent particles and complete spring failure represents crack initiation. Their updated Lagrangian formulation artificially restricts

particle interactions to immediate neighbors without reducing the smoothing length - a simplification that contradicts SPH's fundamental non-local nature and violates the zeroth-order consistency condition of the kernel function. Islam and Peng (Islam & Peng, 2019) was inspired and they implemented a similar spring-based damage model within the TLSPH framework but aforementioned neighborhood restriction remained. Wiragunarsa et al. (Wiragunarsa, Zuhal, Dirgantara & Putra, 2021) developed a TLSPH based fatigue-crack model in which the crack propagation direction is driven by the maximum principal stress between neighboring particles. Moreover, Rahimi and Moutsanidis (Rahimi & Moutsanidis, 2022) coupled TLSPH with the phase-field method - a well-established approach for damage modeling. Their hybrid approach provides greater accuracy for brittle fracture simulation, it comes with significantly higher computational demands compared to other SPH fracture models (Chakraborty & Shaw, 2013; Islam & Peng, 2019; Raymond, Lemiale, Ibrahim & Lau, 2014; Wiragunarsa, Zuhal, Dirgantara & Putra, 2021).

SPH demonstrates robust capabilities in discretizing partial differential operators across both governing equations and constitutive relations. This computational flexibility has led to recognized theoretical parallels with peridynamics and several studies has investigated their connections. Bessa et al. (Bessa, Foster, Belytschko & Liu, 2014) established an important theoretical link by demonstrating that the discretized formulations of peridynamics can be derived through the Reproducing Kernel Particle Method (RKPM) (Liu, Jun & Zhang, 1995), another meshless method developed to improve SPH's accuracy in boundary regions and to restore consistency conditions. Their work revealed how RKPM's kernel correction techniques naturally extend to peridynamic formulations. The relationship between these methods was further clarified by Ganzenmüller et al. (Ganzenmüller, Hiermaier & May, 2015), who performed a rigorous mathematical analysis showing that TLSPH and peridynamics become formally equivalent when expressed in their discretized forms. This equivalence stems from their shared use of non-local interaction models, though they differ in their treatment of deformation states and failure criteria. The theoretical unification of these approaches has important implications for computational mechanics, as it allows for cross-pollination of numerical techniques between the two methods. Building on these fundamental insights, Zhou et al. (Zhou, Yao & Berto, 2021) developed an innovative hybrid framework called Smoothed Peridynamics (SPD) that strategically combines the strengths of both methods. Their approach recognizes that updated Lagrangian SPH is particularly well-suited for modeling large deformations due to its adaptive kernel support, while peridynamics - as an inherently total Lagrangian method with constant neighbor interactions - provides superior capabilities for crack propagation simulations. The SPD formulation main-

tains an updated Lagrangian framework, enabling it to handle finite deformations while incorporating peridynamics-inspired mechanisms for discontinuity modeling. This synthesis creates a powerful computational tool that addresses two of the most challenging aspects of solid mechanics simulations within a unified particle-based framework.

While SPH shows considerable promise for crack propagation applications, its implementation for composite laminates remains relatively underdeveloped. Giannaros et al. (Giannaros, Kotzakolios, Kostopoulos & Campoli, 2019) employed a fully SPH-based approach for an impact problem in which both the projectile and the composite target is modeled via SPH. However, they utilized an updated Lagrangian formulation with variable smoothing length, albeit at significant computational expense. For a similar impact simulation, Cherniaev and Telichev (Cherniaev & Telichev, 2015) adopted a hybrid SPH-FEM methodology, applying SPH solely to the projectile while relying on FEM for the composite plate. Vignjevic et al. (Vignjevic, Vuyst & orevi, 2024) investigated crack propagation in composite structures where they present an interparticle area-reduction criteria for crack propagation into existing models. Karamanli's investigations (Karamanli, 2016; Karamanlı, 2017) of functionally graded materials (including composites) through symmetric SPH formulations demonstrate promising results for elastic deflections under various beam theories, yet these static approaches cannot capture time-dependent behavior under dynamic loading conditions. SPH has found more extensive application in modeling composite manufacturing processes, as demonstrated by He et al. and Huntley et al. (He, Lu, Chen, Li & Lu, 2017; Huntley, Rendall, Longana, Pozegic, Potter & Hamerton, 2020) in their simulations of short fiber-reinforced polymer production. These studies treat polymer melts as weakly compressible SPH fluids while modeling fibers as rigid bodies influenced by flow characteristics. While valuable for process simulation, such applications differ fundamentally from the mechanical behavior analysis of cured composite structures.

1.3 Motivation

The literature review in previous section identifies critical shortcomings in existing SPH formulations for crack propagation modeling. In addition, there is no comprehensive TLSPH study that investigates quasi-static and/or dynamic flexural responses in laminated composite systems. This dissertation addresses these re-

search gaps through two complementary investigations: (i) development of a novel TLSPH damage formulation for isotropic elastic solids, and (ii) implementation of an innovative TLSPH framework for dynamic flexural analysis of composite beam and plate structures.

The first study introduces a novel TLSPH damage formulation designed for isotropic elastic solids to overcome key numerical challenges in fracture modeling. The framework employs a total Lagrangian approach to inherently mitigate tensile instability while incorporating a peridynamics-inspired failure criterion: particle interactions are terminated upon exceeding a *critical stretch* threshold. To address crack-tip singularities and kernel consistency violations, the formulation implements two stabilization techniques: (1) localized enhancement of numerical diffusion and (2) velocity filtering in damaged regions. Fundamental capability of the proposed approach is first demonstrated via large deformation analyses of undamaged 2D and 3D cantilever beams. Subsequently, the damage model's efficacy is investigated against established benchmark problems, including 2D/3D Kalthoff-Winkler experiments and 2D dynamic crack branching scenarios. These test cases systematically verify the method's accuracy in capturing both crack initiation and complex propagation patterns.

The second study introduces a novel application of TLSPH formulation for the three-dimensional macro-modeling of composite laminates, thereby addressing a significant void in the current literature. The proposed methodology utilizes a strong-form governing equation to accurately capture the temporal evolution of the material's mechanical response. By representing each layer as a homogeneous orthotropic material, the approach circumvents the computational demands associated with micro-scale modeling while maintaining efficiency. In contrast to computationally intensive updated Lagrangian SPH formulations, the straightforward TLSPH framework offers an efficient approach. Furthermore, this method diverges from traditional mid-plane theories, such as the First Shear Deformation Theory (FSDT), which treat the entire laminate as a single equivalent layer. Instead, each individual layer is discretized into multiple particles through its thickness, enabling a high-fidelity observation of the mechanical behavior across the thickness. This advancement provides more profound insights into the time-dependent response of laminated composite structures. To ensure comparability with quasi-static conditions, the applied load follows a smooth temporal ramp function, which minimizes numerical instabilities and enhances simulation accuracy. The numerical framework also incorporates hourglass control and artificial viscosity techniques to improve robustness under complex loading scenarios. Validation through numerical examples confirms the accuracy, efficiency, and practical applicability of the proposed method to real-world engineering problems.

2. METHODOLOGY

This chapter presents the theoretical foundations and numerical implementation of the TLSPH framework developed for damage propagation and composite structures. The computational methodology begins by defining the fundamental SPH discretization for vector-valued function and its gradient, establishing the mathematical foundation for subsequent formulations. Building upon this discretization approach, the governing equations of motion are discretized in their total Lagrangian formulation. For the damage modeling part of this research, a constitutive model describing isotropic elastic material behavior and proposed novel damage model are presented. Subsequently, general constitutive model of laminated composite structures is given for analyzing the dynamic flexural behavior of composite beams and plate. This progressive formulation ensures consistent treatment of both isotropic damage propagation and anisotropic composite behavior within the unified TLSPH framework.

To enhance the clarity, a brief overview of the notational conventions is necessary. Particle indices are represented by bold subscripts, $\mathbf{i}$ and $\mathbf{j}$. Vectors and tensors are denoted by boldface symbols, either directly (e.g., $\mathbf{v}$) or using index notation where superscripts indicate the components (e.g., v^k). As an exception, the components of base vectors are indicated by subscripts (e.g., e_k). The magnitude (norm) of a vector is represented by its non-bold counterpart, such that $x_{\mathbf{ij}} = |\mathbf{x_{ij}}|$. To differentiate variables in the initial configuration from those in the deformed configuration, uppercase letters are used for the former.

2.1 SPH Discretization

As stated in Appendix A in which a brief mathematical background of SPH is given, value of a field function f in the spatial coordinate of particle $\mathbf{i}$ can be calculated in

SPH framework as:

$$f(\mathbf{x_i}) \equiv \int_\Omega f(\mathbf{x_j}) W(|\mathbf{x_i} - \mathbf{x_j}|, h) d^3\mathbf{x_j}, \tag{2.1}$$

and the gradient of a field function via SPH kernel approximation is:

$$f'(\mathbf{x_i}) \equiv \int_\Omega f(\mathbf{x_j}) \frac{\partial W(|\mathbf{x_i} - \mathbf{x_j}|, h)}{\partial \mathbf{x_i}} d^3\mathbf{x_j}. \tag{2.2}$$

Here, $\mathbf{x_i}$ and $\mathbf{x_j}$ are coordinate vectors of particle $\mathbf{i}$ and $\mathbf{j}$, respectively. In SPH, each particle $\mathbf{i}$ possesses a compact support domain which is typically defined as a circle (in 2D) or a sphere (in 3D) centered at the particle's location. The radius of this support domain is given by κh, where h represents a parameter that governs the spatial extent of particle interactions and is called "smoothing length", and κ is a dimensionless constant scaling factor. Any other particle $\mathbf{j}$ that lies within the support domain of particle $\mathbf{i}$ is considered a "neighbor" of particle $\mathbf{i}$. Consequently, the support domain of particle $\mathbf{i}$ is also referred to as the "neighborhood" of particle $\mathbf{i}$, encompassing all particles that directly interact with particle $\mathbf{i}$ in the SPH formulation. To improve the readability in this dissertation, $\mathbf{x_i} - \mathbf{x_j}$ (the distance vector between particle $\mathbf{i}$ and particle $\mathbf{j}$), $W(|\mathbf{x_i} - \mathbf{x_j}|, h)$ (the kernel function) and $f(\mathbf{x_i})$ will be denoted as $\mathbf{x_{ij}}$, $W_{\mathbf{ij}}$ and $f_\mathbf{i}$, respectively. In the context of SPH, Equation 2.1 is discretized as:

$$f_\mathbf{i}^s = \sum_{\mathbf{j}=1}^{N} V_\mathbf{j} f_\mathbf{j}^s W_{\mathbf{ij}}, \tag{2.3}$$

where V_j is the volume of particle $\mathbf{j}$ and N is the total number of the neighbors of particle $\mathbf{i}$. It is important to note that directly derivating Equation 2.3 for discretizing the gradient of a function may results in low accuracy. This is primarily attributed to numerical errors arising from non-uniform particle distributions and/or incomplete support domains for particles that are near to the domain boundaries. Thus, corrective SPH formulations are used to prevent this problem (Lin, Naceur, Coutellier & Laksimi, 2014; Shadloo, Zainali, Sadek & Yildiz, 2011). Accordingly, one can express the discretized gradient of a vector-valued function in two different ways as:

$$\frac{\partial f_\mathbf{i}^s}{\partial x_\mathbf{i}^k} \alpha_\mathbf{i}^{kl} = \sum_{\mathbf{j}=1}^{N} V_\mathbf{j} \left(f_\mathbf{j}^s - f_\mathbf{i}^s \right) \frac{\partial W_{\mathbf{ij}}}{\partial x_\mathbf{i}^l}, \tag{2.4}$$

$$\frac{\partial f_\mathbf{i}^s}{\partial x_\mathbf{i}^k} \alpha_\mathbf{i}^{kl} = \sum_{\mathbf{j}=1}^{N} V_\mathbf{j} \left(\frac{f_\mathbf{i}^s}{{\rho_\mathbf{i}}^2} + \frac{f_\mathbf{j}^s}{{\rho_\mathbf{j}}^2} \right) \frac{\partial W_{\mathbf{ij}}}{\partial x_\mathbf{i}^l}. \tag{2.5}$$

In above equations, $\alpha_{\mathbf{i}}^{sl}$ is the correction tensor:

$$\alpha_{\mathbf{i}}^{sl} = \sum_{\mathbf{j}=1}^{N} \mathbf{x}_{\mathbf{ji}}^{s} V_{\mathbf{j}} \frac{\partial W_{\mathbf{ij}}}{\partial x_{\mathbf{i}}^{l}}. \tag{2.6}$$

To compute the gradients of function that are at the right hand side of Equation 2.4 an Equation 2.5, the correction tensor must be inversed and added to the left hand side of the equations. Multiplying the inverse of the correction tensor with the gradient of the kernel function gives "corrected kernel gradient" and it is denoted as $\widetilde{\nabla} W_{\mathbf{ij}} = (\mathbf{A_i})^{-1} \nabla W_{\mathbf{ij}}$, where $\mathbf{A_i}$ and $\nabla W_{\mathbf{ij}}$ are $\left(\alpha_{\mathbf{i}}^{sl}\right)^{-1}$ and $\partial W_{\mathbf{ij}}/\partial x_{\mathbf{i}}^{l}$, respectively.

The choice of kernel function plays a critical role in SPH formulations since it influences accuracy, stability, and computational efficiency of the simulation. While various kernel formulations exist in the literatureincluding Gaussian, quartic, and quintic spline functionsthis study adopts the cubic spline kernel (Liu & Liu, 2010; Shadloo, Zainali & Yildiz, 2013) for its optimal balance between numerical stability and computational practicality. The cubic kernel is defined as:

$$W(q,h) = a_d \begin{cases} \frac{2}{3} - q^2 + \frac{1}{2}q^3, & 0 \leq q < 1 \\ \frac{1}{6}(2-q)^3, & 1 \leq q \leq 2 \\ 0, & q > 2. \end{cases} \tag{2.7}$$

where a_d is the kernel normalization factor and it is equal to $15/(7\pi h^2)$ or $3/(2\pi h^3)$ for 2D and 3D simulations, respectively. q is set to $x_{\mathbf{ij}}/h$ and h equals to some coefficient such as 1.33 or 2 times the initial particle distance Δx.

2.2 Governing Equations

The theoretical foundation of the TLSPH formulation starts with two fundamental conservation equations and their discretization according to the Lagrangian description of motion. For solid mechanics applications, the governing equations are expressed in terms of the material derivative to track the motion in the reference configuration. Accordingly, the conservation of mass and linear momentum are:

$$\frac{d\rho}{dt} = -\rho \nabla \cdot \mathbf{v}, \tag{2.8}$$

$$\frac{d\mathbf{v}}{dt} = \frac{1}{\rho}\nabla \cdot \boldsymbol{\sigma} + \mathbf{b}, \tag{2.9}$$

where ρ, $\mathbf{v}$, $\mathbf{b}$ and $\boldsymbol{\sigma}$ denote the density, the velocity vector and external force per unit mass and Cauchy stress tensor, respectively. According to the total Lagrangian description, the conservation of mass (Equation 2.8) can be achieved by updating the density simply with a linear algebraic equation. According to the total Lagrangian description, the deformed material coordinates $\mathbf{x}$ and undeformed coordinates $\mathbf{X}$ are related by the displacement vector $\mathbf{u} = \mathbf{x} - \mathbf{X}$. In addition, conservation of linear momentum (Equation 2.9) can be re-written by replacing Cauchy stress tensor $\boldsymbol{\sigma}$ with the first Piola-Kirchhoff stress tensor $\mathbf{P}$. Thus, Equation 2.8 and Equation 2.9 becomes:

$$\rho = \frac{\rho_0}{J}, \tag{2.10}$$

$$\frac{d\mathbf{v}}{dt} = \frac{1}{\rho_0}\nabla_0 \cdot \mathbf{P} + \mathbf{b}, \tag{2.11}$$

Here, $\mathbf{P}$ is the first Piola-Kirchoff tensor and it is computed either by mapping Cauchy stress tensor to the undeformed (reference) configuration or with second Piola-Kirchoff tensor $\mathbf{S}$ using deformation gradient $\mathbf{F} = \partial\mathbf{x}/\partial\mathbf{X}$, depending on the simulation scenario. $\mathbf{J}$ is the Jacobian and it is equal to determinant of the deformation gradient tensor and the subscript 0 is used to indicate the reference configuration. Regardless of how $\mathbf{P}$ is calculated, one needs to compute Green-Lagrange strain tensor as:

$$\mathbf{E} = \frac{1}{2}\left(\mathbf{L} + \mathbf{L}^T + \mathbf{L}^T\mathbf{L}\right), \tag{2.12}$$

where $\mathbf{L}$ is the displacement gradient tensor and it is equal to $\partial\mathbf{u}/\partial\mathbf{X}$. In TLSPH context, $\mathbf{F}$ and $\mathbf{L}$ can be discretized using Equation 2.4 as below:

$$\mathbf{F} = \left(\frac{\partial\mathbf{x}}{\partial\mathbf{X}}\right)_i = \sum_{\mathbf{j}=1}^{N}(\mathbf{x_j} - \mathbf{x_i})\widetilde{\nabla}_0 W_{\mathbf{ij}} V_0, \tag{2.13}$$

$$\mathbf{L} = \left(\frac{\partial\mathbf{u}}{\partial\mathbf{X}}\right)_i = \sum_{\mathbf{j}=1}^{N}(\mathbf{u_j} - \mathbf{u_i})\widetilde{\nabla}_0 W_{\mathbf{ij}} V_0. \tag{2.14}$$

For discretization of conservation of linear momentum equation, Equation 2.5 is utilized since it performs better for stress derivatives. To this extent, Equation 2.11

is discretized as:

$$\left(\frac{d\mathbf{v}}{dt}\right)_{\mathbf{i}} = \sum_{\mathbf{j}=1}^{N} \rho_0 \left(\frac{\mathbf{P_i}}{\rho_{\mathbf{i}}^2} + \frac{\mathbf{P_j}}{\rho_{\mathbf{j}}^2}\right) \widetilde{\nabla}_0 W_{\mathbf{ij}} V_0 + \mathbf{b_i}. \tag{2.15}$$

2.2.1 Stabilization Techniques

Several stabilization techniques that form the backbone the novelty of the studies are utilized. Firstly, to eliminate the numerical instabilities driven by the non-physical shock-wave oscillations, the artificial viscosity stress term $\mathbf{P}_{\nu\mathbf{ij}}$ is included as a stabilization technique. Therefore, Equation 2.15 becomes:

$$\left(\frac{d\mathbf{v}}{dt}\right)_{\mathbf{i}} = \sum_{\mathbf{j}=1}^{N} \rho_0 \left(\frac{\mathbf{P_i}}{\rho_{\mathbf{i}}^2} + \frac{\mathbf{P_j}}{\rho_{\mathbf{j}}^2} - \mathbf{P}_{\nu\mathbf{ij}}\right) \widetilde{\nabla}_0 W_{\mathbf{ij}} V_0 + \mathbf{b_i}. \tag{2.16}$$

The artificial viscosity stress term is fist computed in deformed configuration as:

$$\Pi_{\mathbf{ij}} = \begin{cases} \frac{-\alpha_{\mathbf{i}} \mu_{\mathbf{ij}} c_0 + \beta \mu_{ij}^2}{\rho_0}, & (\mathbf{v_i} - \mathbf{v_j}) \cdot (\mathbf{X_i} - \mathbf{X_j}) < 0, \\ 0, & (\mathbf{v_i} - \mathbf{v_j}) \cdot (\mathbf{X_i} - \mathbf{X_j}) \geq 0, \end{cases} \tag{2.17}$$

where $\mu_{\mathbf{ij}}$ is;

$$\mu_{\mathbf{ij}} = \frac{h(\mathbf{v_i} - \mathbf{v_j}) \cdot (\mathbf{X_i} - \mathbf{X_j})}{\left|\mathbf{X_i} - \mathbf{X_j}\right|^2 + 0.01h^2}. \tag{2.18}$$

$c_0 = \sqrt{\left(\kappa + \frac{4\mu}{3}\right)/\rho}$ is the speed of the sound in solids in which $\kappa = \lambda + (2/3)\mu$ is the bulk modulus. $\Pi_{\mathbf{ij}}$ is then mapped to the undeformed configuration according to the below relation:

$$\mathbf{P}_{\nu\mathbf{ij}} = det(\mathbf{F}) \Pi_{\mathbf{ij}} \mathbf{F}^{-T}. \tag{2.19}$$

Another stabilization technique used in this research is based on the study of Ganzenmüller et al. (Ganzenmüller, 2015). According to his elaboration, the correction tensor that is used to correct the kernel gradient is not symmetric particle wise, $\mathbf{A_i} \neq \mathbf{A_j}$. This is mainly due to incomplete support domains of particles near the domain boundaries. Thus, the property of antisymmetry is no longer held i.e, $\widetilde{\nabla} W_{\mathbf{ij}} \neq -\widetilde{\nabla} W_{\mathbf{ji}}$, which results in the violation of the conservation of the linear momentum. To prevent this inconsistency, a modification in Equation 2.16 is made as

below:

$$\left(\frac{d\mathbf{v}}{dt}\right)_{\mathbf{i}} = \sum_{\mathbf{j}=1}^{N} \rho_0 V_0 \left(\frac{\mathbf{P_i}}{\rho_{\mathbf{i}}^2}\widetilde{\nabla}_0 W_{\mathbf{ij}} - \frac{\mathbf{P_j}}{\rho_{\mathbf{j}}^2}\widetilde{\nabla}_0 W_{\mathbf{ji}} - \mathbf{P}_{\nu\mathbf{ij}}\widetilde{\nabla}_0 W_{\mathbf{ij}}\right) + \mathbf{b_i}. \tag{2.20}$$

For small to moderate deformations, the aforementioned stabilization techniques applied within the discretized acceleration equation (Equation 2.20) typically provide sufficient accuracy. However, when evaluating the in-house TLSPH code under large deformation scenarios, the occurrence of unphysical particle clustering is observed. This instability is found to be a phenomenon analogous to hourglass problem in FEM. In FEM, hourglassing arises from the use of an insufficient number of integration points within an element, leading to spurious zero-energy modes of deformation where elements deform without a corresponding strain energy. From SPH point of view, center of the SPH particle can be considered as an integration point and the kernel function filters the value of any field variable through neighboring particles with a linear deformation gradient tensor $\mathbf{F}$. This interpolation can struggle to accurately represent complex deformation states under non-linear behaviors. To this end, Ganzenmüller et al. (Ganzenmüller, 2015) proposed a virtual "hourglass force" to mitigate the incorrect deformation representation. Since both crack propagation and composite modeling studies involve many non-linearities, hourglass force term is included in both. The hourglass force formulation begins by definining an error vector $\boldsymbol{\mathcal{E}}_{ij}$ between the actual and mapped distance vector in deformed configuration as below:

$$\mathcal{E}_{\mathbf{ij}} = \mathbf{x_{ij}} - \mathbf{F_i}\mathbf{X_{ij}}. \tag{2.21}$$

Error vector $\boldsymbol{\mathcal{E}}_{ij}$ can be minimized by correcting the distance vector $\mathbf{x_{ij}}$. The hourglass correction force $\mathbf{f}_{HG}$ is:

$$\mathbf{f}_{HG} = -\frac{\gamma E}{\rho_0}\sum_{\mathbf{j}=1}^{N} V_{\mathbf{j}}\left[\frac{\delta_{\mathbf{ij}} + \delta_{\mathbf{ji}}}{2}\right]\frac{\mathbf{x_{ij}}}{X_{\mathbf{ij}}^2 x_{\mathbf{ij}}} W_{\mathbf{ij}}, \tag{2.22}$$

where γ is a coefficient for adjusting the magnitude of $\mathbf{f}_{HG}$. Its value is chosen to minimize the ratio of hourglass energy to the total system energy. This selection ensures that non-physical deformation modes are effectively mitigated without compromising the physical accuracy of the results. This minimization process is conducted using a systematic trial-and-error approach. In this method, a range of parameter values are manually tested to identify the configuration that yielded stable and physically consistent results (Ganzenmüller, 2015). The simulation results are made to demonstrate close agreement with those obtained from established com-

mercial finite element package keeping the hourglass energy as a small fraction of the total internal energy as possible. $\delta_{\mathbf{ij}}$ is defined for minimizing the error vector $\boldsymbol{\mathcal{E}}_{ij}$ by correcting the distance between particle i and particle j as:

$$\delta_{\mathbf{ij}} = \frac{\mathcal{E}_{\mathbf{ij}} \cdot \mathbf{x_{ij}}}{x_{\mathbf{ij}}}. \tag{2.23}$$

Incorporating $\mathbf{f}_{HG}$ in Equation 2.20 results in final form of discretized version of the conservation of the linear momentum:

$$\left(\frac{d\mathbf{v}}{dt}\right)_{\mathbf{i}} = \sum_{\mathbf{j}=1}^{N} \rho_0 V_0 \left(\frac{\mathbf{P_i}}{\rho_{\mathbf{i}}^2}\widetilde{\nabla}_0 W_{\mathbf{ij}} - \frac{\mathbf{P_j}}{\rho_{\mathbf{j}}^2}\widetilde{\nabla}_0 W_{\mathbf{ji}} - \mathbf{P}_{\nu\mathbf{ij}}\widetilde{\nabla}_0 W_{\mathbf{ij}}\right) + \mathbf{f}_{HG\mathbf{i}} + \mathbf{b_i}, \tag{2.24}$$

which the code solves at the end of the each time step. The formulation scheme detailed thus far is common to both research endeavors within this dissertation. However, the calculation of the first Piola-Kirchhoff stress tensor, $\mathbf{P}$, varies depending on the scenarios investigated within this dissertation.

2.3 A Novel TLSPH Approach for Modeling Damage in Elastic Solids

In this section, the constitutive relations for a linearly elastic isotropic body are explained and the novel damage model is presented. For the modeling of the crack propagation case, the second Piola-Kirchhoff stress tensor is employed due to its demonstrated capacity to provide enhanced accuracy in the results:

$$\mathbf{S} = \lambda tr(\mathbf{E})\mathbf{I} + 2\mu\mathbf{E}, \tag{2.25}$$

where $\mu = E/2(\nu+1)$ and $\lambda = E\nu/((1+\nu)(1-2\nu))$ are Lamé constants in which E and ν are the elasticity modulus and Poisson's ratio and $\mathbf{I}$ is the identity tensor. The first Piola-Kirchhoff stress tensor is then computed as:

$$\mathbf{P} = \mathbf{FS} \tag{2.26}$$

2.3.1 Novel Damage Model

Despite the methodological differences between peridynamics and the classical continuum mechanics approach of TLSPH, their final discretized forms exhibit notable correspondence as explained by Ganzenmüller et al. (Ganzenmüller, Hiermaier & May, 2015). The damage criterion in bond-based peridynamics is solely based on the material properties and particle influence radius (which is equivalent to smoothing length in SPH). Based on these information, adopting this damage model into TLSPH context can be rational. Therefore, the proposed damage model's criterion is directly inspired by peridynamics theory, which is elaborated in Madenci's book (Madenci & Oterkus, 2013). It's important to note that the bond-based formulation that we are inspired, which employs a constant support domain, is specifically for linear elastic isotropic solids. For heterogeneous materials or more complex material behaviors, the Dual-Horizon peridynamics formulation, as presented in (Ren, Zhuang & Rabczuk, 2017), may be a more suitable approach.

The novel damage model begins by defining a strain variable $\mathbf{s_{ij}}$ between two particles as:

$$\mathbf{s_{ij}} = \frac{|X_{\mathbf{ij}} - x_{\mathbf{ij}}|}{|X_{\mathbf{ij}}|}. \tag{2.27}$$

In peridynamics literature, $\mathbf{s_{ij}}$ is called *stretch* and the distance vector between two particles is called *bond*. Stretch characterizes the change in the length of the bond through undeformed to deformed state between particle **i** and particle **j**. Similarly, *critical stretch* $\mathbf{s_c}$ that denotes the maximum allowable strain for a particle pair is expressed as:

$$s_c = \begin{cases} \sqrt{\dfrac{G_c}{\left(3\mu + \left(\frac{3}{4}\right)^4 \left(\kappa - \frac{5\mu}{3}\right)\right)\delta}}, & \text{for 3 dimensions,} \\ \sqrt{\dfrac{G_c}{\left(\frac{6\mu}{\pi} + \frac{16}{9\pi^2}(\kappa - 2\mu)\right)\delta}}, & \text{for 2 dimensions,} \end{cases} \tag{2.28}$$

where G_c is the critical energy release rate and δ is peridynamics' *horizon* that is conceptually equivalent to SPH's smoothing length h. Once the stretch between two particles exceeds the critical stretch, their interaction is terminated, i.e. the bond is broken, by embedding a binary-valued variable $\lambda_{\mathbf{ij}}$ into the equations:

$$\lambda_{\mathbf{ij}} = \begin{cases} 1, & s_{\mathbf{ij}} < s_c, \\ 0, & s_{\mathbf{ij}} \geq s_c. \end{cases} \tag{2.29}$$

Thus, Equation 2.13, Equation 2.14 and Equation 2.24 are modified as follows;

$$\mathbf{F_i} = \left(\frac{\partial \mathbf{x}}{\partial \mathbf{X}}\right)_\mathbf{i} = \sum_{\mathbf{j}=1}^{N} \lambda_\mathbf{ij} V_\mathbf{j} (\mathbf{x_j} - \mathbf{x_i}) \widetilde{\nabla}_0 W_\mathbf{ij}, \tag{2.30}$$

$$\mathbf{L_i} = \left(\frac{\partial \mathbf{u}}{\partial \mathbf{X}}\right)_\mathbf{i} = \sum_{\mathbf{j}=1}^{N} \lambda_\mathbf{ij} V_\mathbf{j} (\mathbf{u_j} - \mathbf{u_i}) \widetilde{\nabla}_0 W_\mathbf{ij}, \tag{2.31}$$

$$\left(\frac{d\mathbf{v}}{dt}\right)_\mathbf{i} = \sum_{\mathbf{j}=1}^{N} \lambda_\mathbf{ij} \rho_\mathbf{j} V_\mathbf{j} \left(\frac{\mathbf{P_i}}{\rho_\mathbf{i}^2} \widetilde{\nabla}_0 W_\mathbf{ij} - \frac{\mathbf{P_j}}{\rho_\mathbf{j}^2} \widetilde{\nabla}_0 W_\mathbf{ji} - \mathbf{P}_{\nu\mathbf{ij}} \widetilde{\nabla}_0 W_\mathbf{ij}\right) + \mathbf{f}_{HG\mathbf{i}} + \mathbf{b_i}. \tag{2.32}$$

To be able to characterize the quantity of the damage that ranges between 0 (no damage) and 1 (completely damaged), the ratio of the number of the broken bonds to the total number of the bonds $\phi_\mathbf{i}$ can be defined as:

$$\phi_\mathbf{i} = 1 - \frac{\sum_{\mathbf{j}=1}^{N} \lambda_\mathbf{ij}}{N}. \tag{2.33}$$

To obtain a smoother and more diffusive damage representation, $\phi'_\mathbf{i}$ is used instead as:

$$\phi'_\mathbf{i} = \phi_\mathbf{i} - \frac{\sum_{\mathbf{j}=1}^{N} (\phi_\mathbf{i} - \phi_\mathbf{j}) W_\mathbf{ij}}{\sum_{\mathbf{j}=1}^{N} W_\mathbf{ij}} \tag{2.34}$$

2.3.1.1 Suppressing of damage related instabilities

Once the stretch of a bond exceeds its critical stretch threshold, the bond is considered broken. This means that particle **j** is eliminated from the neighborhood of particle **i** and particle **j** no longer contributes to the kernel interpolation of any field variable on particle **i**. As explained in Appendix A, the kernel function must satisfy below relations:

- The normalization condition ($\sum_{\mathbf{j}=1}^{N} \lambda_\mathbf{ij} V_\mathbf{j} W_\mathbf{ij} = 1$) which is necessary for precise computation of displacement and velocity field
- The derivation of normalization condition ($\sum_{\mathbf{j}=1}^{N} \lambda_\mathbf{ij} V_\mathbf{j} \nabla W_\mathbf{ij} = 0$) which ensures accurate stress field approximation

After the neighbor eliminations, both of the above expressions are violated which results in rank deficiency problem, explained in introduction. Furthermore, singularities due to the existence of crack arise. To mitigate these singularities, we come up with the idea of increasing the local numerical diffusion by altering the artificial viscosity coefficient α_i according to the below condition:

$$\alpha_i = \begin{cases} \alpha_d, & \phi'_{\mathbf{i}} > 0, \\ \alpha_0, & \phi'_{\mathbf{i}} = 0. \end{cases} \tag{2.35}$$

Besides, the velocity field is smoothed to prevent the unphysical jumps (Ozbulut, Tofighi, Goren & Yildiz, 2017) when a critical damage value is reached, i.e., $\phi_{\mathbf{i}} > \phi_c$:

$$v'_{\mathbf{i}} = v_{\mathbf{i}} - \epsilon \frac{\sum_{\mathbf{j}=1}^{N} (v_{\mathbf{i}} - v_{\mathbf{j}}) W_{\mathbf{ij}}}{\sum_{\mathbf{j}=1}^{N} W_{\mathbf{ij}}}, \tag{2.36}$$

in which ϵ is a velocity smoothing parameter.

Up to this point, there are various equations are given. To enhance the reader's experience, Algorithm 1 can be followed step by step for every procedure for the crack propagation problem.

2.4 Constitutive Model for Composite Modeling

For the composite modeling, the computation of the first Piola-Kirchhoff tensor is achieved by directly mapping of the Cauchy stress tensor $\boldsymbol{\sigma}$ into undeformed configuration, using deformation gradient tensor $\mathbf{F}$ as $\mathbf{P} = det(\mathbf{F})\boldsymbol{\sigma}\mathbf{F}^{-T}$.

In composite laminates, individual plies exhibit anisotropic mechanical properties, initially characterized within a local coordinate system that aligns with the specific fiber orientation of each layer. For a precise analysis of the laminate's global response, these properties must be transformed into a common global coordinate system. Customarily, this involves two frames of reference: a fixed global system (x, y, z) applicable to the entire structure, and a local system (x_1, x_2, x_3) unique to each layer, which is oriented with the fiber direction to account for the material's inherent anisotropy (Figure 2.1). To establish the relationship between the stress and strain within each layer and the overall global structural behavior, the global

Algorithm 1 Code algorithm for the crack propagation problem

Initialize the geometry
Impose the boundary conditions
Perform neighbor search
Set λ_{ij} to 0 for the initial cracks (if present)
Compute $W_{\mathbf{ij}}$ and $\widetilde{\nabla}_0 W_{\mathbf{ij}}$
while $t = 0 <$ *Total Time* **do**
    Compute $\mathbf{F_i}$ and $\mathbf{L_i}$ via Equation 2.30 and Equation 2.31
    Compute $\mathbf{E_i}$ via Equation 2.12
    Compute $\mathbf{S_i}$ via Equation 2.25
    Compute $\mathbf{P_i}$ via Equation 2.26
    Compute $\mathcal{E}_{\mathbf{ij}}$ and $\delta_{\mathbf{ij}}$ via Equation 2.21 Equation 2.23
    Compute $\mathbf{f}_{HG\mathbf{i}}$ via Equation 2.22
    if ${\phi'_{\mathbf{i}}}^n > 0$ **then**
        Compute $\mathbf{P}_{\nu\mathbf{ij}}$ with α_d via Equation 2.19
    else
        Compute $\mathbf{P}_{\nu\mathbf{ij}}$ with α_0 via Equation 2.19
    end if
    Compute $\frac{d\mathbf{v_i}}{dt}$ via Equation 2.32
    Update the velocity ${\mathbf{v}_\mathbf{i}}^{n+1} = {\mathbf{v}_\mathbf{i}}^n + \frac{d\mathbf{v_i}}{dt}\Delta t$
    if ${\phi_\mathbf{i}}^n > \phi_c$ **then**
        Apply velocity smoothing via Equation 2.36
    end if
    Update the displacement ${\mathbf{u}_\mathbf{i}}^{n+1} = {\mathbf{u}_\mathbf{i}}^n + {\mathbf{v}_\mathbf{i}}^{n+1}\Delta t$
    Update the position ${\mathbf{x}_\mathbf{i}}^{n+1} = \mathbf{X_i} + {\mathbf{u}_\mathbf{i}}^{n+1}$
    Compute stretch $\mathbf{s_{ij}}$ via Equation 2.27
    if $\mathbf{s_{ij}} \geq \mathbf{s_c}$ **then**
        Set λ_{ij} to 0
    else
        Set λ_{ij} to 1
    end if
    Compute damage $\phi_\mathbf{i}^{n+1}$ via Equation 2.33
    Compute smoothed damage ${\phi'_\mathbf{i}}^{n+1}$ via Equation 2.34
    Update the time $t^{n+1} = t^n + \Delta t$
    $n \leftarrow n+1$
end while

constitutive matrix $\mathbf{D}^{(k)}$ for the kth layer is employed. This matrix facilitates the connection between the global Cauchy stress tensor of kth layer, $\boldsymbol{\sigma}^{(k)}$, and the global strain tensor of kth layer, $\boldsymbol{\epsilon}^{(k)}$, as defined:

$$\boldsymbol{\sigma}^{(k)} = \mathbf{D}^{(k)}\boldsymbol{\epsilon}^{(k)}, \tag{2.37}$$

and the Cauchy strain tensor $\boldsymbol{\epsilon}$ is:

$$\boldsymbol{\epsilon} = \mathbf{F}^{-\mathbf{T}}\mathbf{E}\mathbf{F}^{\mathbf{T}} \tag{2.38}$$

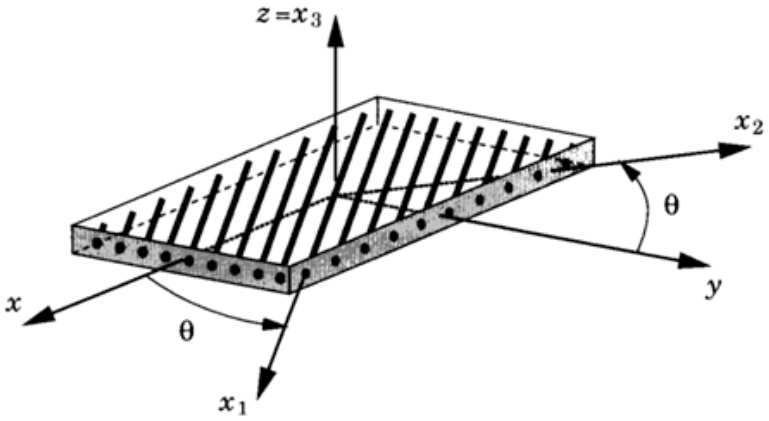

Figure 2.1 Illustration of the coordinate system of the layer of a composite structure (Reddy, 2004)

The explicit form of Equation 2.37 is written as:

$$\begin{Bmatrix} \sigma_{xx} \\ \sigma_{yy} \\ \sigma_{zz} \\ \tau_{xz} \\ \tau_{yz} \\ \tau_{xy} \end{Bmatrix} = \begin{bmatrix} \bar{Q}_{11} & \bar{Q}_{12} & \bar{Q}_{13} & 0 & 0 & \bar{Q}_{16} \\ \bar{Q}_{12} & \bar{Q}_{22} & \bar{Q}_{23} & 0 & 0 & \bar{Q}_{26} \\ \bar{Q}_{13} & \bar{Q}_{23} & \bar{Q}_{33} & 0 & 0 & \bar{Q}_{36} \\ 0 & 0 & 0 & \bar{Q}_{44} & \bar{Q}_{45} & 0 \\ 0 & 0 & 0 & \bar{Q}_{45} & \bar{Q}_{55} & 0 \\ \bar{Q}_{16} & \bar{Q}_{26} & \bar{Q}_{36} & 0 & 0 & \bar{Q}_{66} \end{bmatrix} \begin{Bmatrix} \epsilon_{xx} \\ \epsilon_{yy} \\ \epsilon_{zz} \\ \gamma_{xz} \\ \gamma_{yz} \\ \gamma_{xy} \end{Bmatrix}. \tag{2.39}$$

Here, $\mathbf{D}^{(k)}$ is also expressed as *reduced transformed stiffness matrix* and it is computed by the transformation of local coordinates in global coordinates by using the transformation matrix $\mathbf{T}^{(k)}$ as:

$$\mathbf{D}^{(k)} = \mathbf{T}^{(k)} \tilde{\mathbf{D}}^{(k)} {\mathbf{T}^{(k)}}^{T}. \tag{2.40}$$

$\mathbf{T}^{(k)}$ is defined as:

$$\mathbf{T}^{(k)} = \begin{bmatrix} c^2 & s^2 & 0 & 0 & 0 & -2sc \\ s^2 & c^2 & 0 & 0 & 0 & 2sc \\ 0 & 0 & 1 & 0 & 0 & 0 \\ 0 & 0 & 0 & c & -s & 0 \\ 0 & 0 & 0 & s & c & 0 \\ sc & -sc & 0 & 0 & 0 & c^2 - s^2 \end{bmatrix}, \tag{2.41}$$

in which c and s denote $\cos\theta$ and $\sin\theta$, respectively where θ being the angle between the x_1 and x coordinate axes. Furthermore, $\tilde{\mathbf{D}}^{(k)}$ is the local constitutive matrix

and it is defined as:

$$\tilde{\mathbf{D}}^{(k)} = \begin{bmatrix} Q_{11} & Q_{12} & Q_{13} & 0 & 0 & 0 \\ Q_{12} & Q_{22} & Q_{23} & 0 & 0 & 0 \\ Q_{13} & Q_{23} & Q_{33} & 0 & 0 & 0 \\ 0 & 0 & 0 & G_{13} & 0 & 0 \\ 0 & 0 & 0 & 0 & G_{23} & 0 \\ 0 & 0 & 0 & 0 & 0 & G_{12} \end{bmatrix}. \tag{2.42}$$

Elements of $\tilde{\mathbf{D}}^{(k)}$ are function of elastic moduli $\mathrm{E}_i^{(k)}$, shear moduli $\mathrm{G}_{ij}^{(k)}$ and Poisson ratio $\nu_{ij}^{(k)}$. Note that the subscripts here denote longitudinal (1) or transverse (2,3) directions. These relations are:

$$\begin{aligned} Q_{11}^{(k)} &= E_1^{(k)} \frac{1-\nu_{23}^{(k)}\nu_{32}^{(k)}}{\Delta^{(k)}} \\ Q_{12}^{(k)} &= E_1^{(k)} \frac{\nu_{21}^{(k)}+\nu_{31}^{(k)}\nu_{23}^{(k)}}{\Delta^{(k)}} \\ Q_{13}^{(k)} &= E_3^{(k)} \frac{\nu_{13}^{(k)}+\nu_{12}^{(k)}\nu_{23}^{(k)}}{\Delta^{(k)}} \\ Q_{22}^{(k)} &= E_2^{(k)} \frac{1-\nu_{13}^{(k)}\nu_{31}^{(k)}}{\Delta^{(k)}} \\ Q_{23}^{(k)} &= E_3^{(k)} \frac{\nu_{23}^{(k)}+\nu_{21}^{(k)}\nu_{13}^{(k)}}{\Delta^{(k)}} \\ Q_{33}^{(k)} &= E_3^{(k)} \frac{1-\nu_{12}^{(k)}\nu_{21}^{(k)}}{\Delta^{(k)}}, \end{aligned} \tag{2.43}$$

in which $\Delta^{(k)}$ is:

$$\Delta^{(k)} = 1-\nu_{12}^{(k)}\nu_{21}^{(k)}-\nu_{23}^{(k)}\nu_{32}^{(k)}-\nu_{31}^{(k)}\nu_{13}^{(k)}-2\nu_{21}^{(k)}\nu_{32}^{(k)}\nu_{13}^{(k)}. \tag{2.44}$$

Algorithm 2 is provided to facilitate a clearer understanding of the subsequent equations.

Algorithm 2 Code algorithm for composite modeling

Initialize the geometry with material properties
Compute $\tilde{\mathbf{D}}^{(k)}$ and $\mathbf{T}^{(k)}$ via Equation 2.42 and Equation 2.41
Compute $\mathbf{D}^{(k)}$ via Equation 2.40
Impose the boundary conditions
Perform the neighbor search
Compute $W_{\mathbf{ij}}$ and $\widetilde{\nabla}_0 W_{\mathbf{ij}}$
while $t = 0 <$ *Total Time* **do**
    Compute $\mathbf{F}_i$ and $\mathbf{L}_i$ via Equation 2.13 and Equation 2.14
    Compute $\mathbf{E}_i$ via Equation 2.12
    Compute $\boldsymbol{\epsilon}_i$ via Equation 2.38
    Compute $\boldsymbol{\sigma}_i^{(k)}$ via Equation 2.37
    Compute $\mathbf{P_i} = det(\mathbf{F_i})\boldsymbol{\sigma}_\mathbf{i}\mathbf{F}_\mathbf{i}^{-T}$
    Compute $\mathcal{E}_{\mathbf{ij}}$ then $\delta_{\mathbf{ij}}$ via Equation 2.21 and Equation 2.23
    Compute $\mathbf{f}_{HG\mathbf{i}}$ via Equation 2.22
    Compute $\mu_{\mathbf{ij}}$ and $\Pi_{\mathbf{ij}}$ via Equation 2.18 and 2.17
    Compute $\mathbf{P}_{\nu\mathbf{ij}}$ via Equation 2.19
    Compute $\left(\frac{d\mathbf{v}}{dt}\right)_\mathbf{i}$ via Equation 2.24
    Update the velocity $\mathbf{v}_\mathbf{i}^{n+1} = \mathbf{v}_\mathbf{i}^n + \left(\frac{d\mathbf{v}}{dt}\right)_\mathbf{i} \Delta t$
    Update the displacement $\mathbf{u}_\mathbf{i}^{n+1} = \mathbf{u}_\mathbf{i}^n + \mathbf{v}_\mathbf{i}^{n+1}\Delta t$
    Update the position $\mathbf{x}_\mathbf{i}^{n+1} = \mathbf{X_i} + \mathbf{u}_\mathbf{i}^{n+1}$
    Update the time $t^{n+1} = t^n + \Delta t$
    $n \leftarrow n + 1$
end while

3. RESULTS AND DISCUSSION

This section provides results and their corresponding discussion for various simulations. All simulations are modeled within in-house C++ code which is parallelized via CUDA.

Firstly, a brand new C++ code based on TLSPH formulation is developed and its capability is verified through simulation of a cantilever beam undergoing large deformation in 2D and 3D. Then, the results of the first study, A Novel TLSPH Approach for Modeling Damage in Elastic Solids, is given for two different benchmark cases: Simulation of Kalthoff-Winkler and dynamic crack branching experiments.

This dissertation makes a significant contribution by applying the TLSPH method to the deformation analysis of composite beams and plates, thereby addressing a notable gap in the existing literature.

3.1 Large Deformation of a Cantilever Beam

To validate the in-house TLSPH code's performance in large deformation problems, we simulated the deflection of a cantilever beam under transverse loading in both 2D and 3D. We then compared our results against existing studies by He et al. (He, Tofighi, Yildiz, Lei & Suleman, 2017) and (He & Lei, 2019), respectively.

The initial discretization involved uniformly separated particles with a spatial resolution Δx of 0.001 m. A transverse force of 17.5 kN is applied at the beam's tip, imposed as an external force per unit particle mass into Equation 2.32, ensuring the total external force per unit mass remained consistent for both 2D and 3D simulations. The time step Δt is determined by the Courant-Friedrichs-Lewy (CFL) condition, $\Delta t \leq C_{CFL}\,(h/c_0)$ with C_{CFL} set to 0.16. For stabilization, the hourglass correction force coefficient is set to 1.0, while the artificial viscosity coefficients α

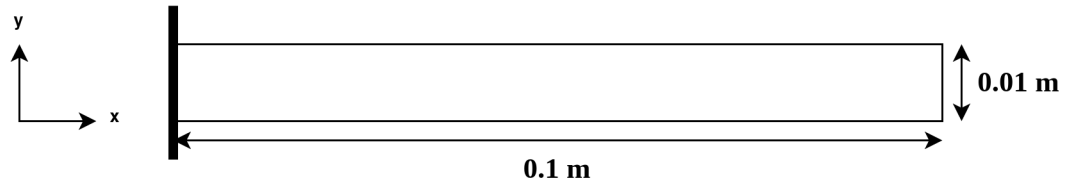

Figure 3.1 2D cantilever beam.

and β are 0.002 and 0, respectively. Table 3.1 outlines the material properties used in these simulations.

Table 3.1 Material properties for cantilever beam.

Parameter	**Young's Modulus**	**Density**	**Poisson Ratio**
Value	210 GPa	7800kg/m^3	0.3

3.1.1 2D Cantilever Beam Simulation

The geometry of the 2D cantilever beam is depicted in Figure 3.1. This beam has a thickness (d) of 0.001 m and is discretized into a total of 1000 particles. To enforce the clamped boundary condition at the beam's left end, the accelerations of the first three columns of particles are constrained to zero throughout the simulation. A transverse force is applied at the central particle of the beam tip in the negative y-direction. This force increases linearly from t = 0 s to t = 1 s, then remains constant until t = 2 s. The mass of each particle is assumed to be $\rho(\Delta x)^2 d$, with the corresponding external acceleration term, $b_{\mathbf{i}}$, presented in Equation 3.1.

$$b_i(t) = \begin{cases} \dfrac{17500t}{\rho(\Delta x)^2 d}, & t < 0.5\,\mathrm{s}, \\ \dfrac{17500}{\rho(\Delta x)^2 d}, & 0.5 \leq t \leq 1.0\,\mathrm{s}, \end{cases} \tag{3.1}$$

Figure 3.2 presents the simulation outcomes. Specifically, Figure 3.2a displays the time history of the vertical displacement at the beam's tip. A comparison with the TLSPH and FEM results from He et al. (He, Tofighi, Yildiz, Lei & Suleman, 2017) clearly demonstrates the close alignment of the present study's findings. Furthermore, Figure 3.2b illustrates the deformed configuration of the 2D cantilever beam at t = 2 s. These results exhibit a smooth displacement field, notably free from unphysical particle separations or clusters, which underscores the effectiveness of

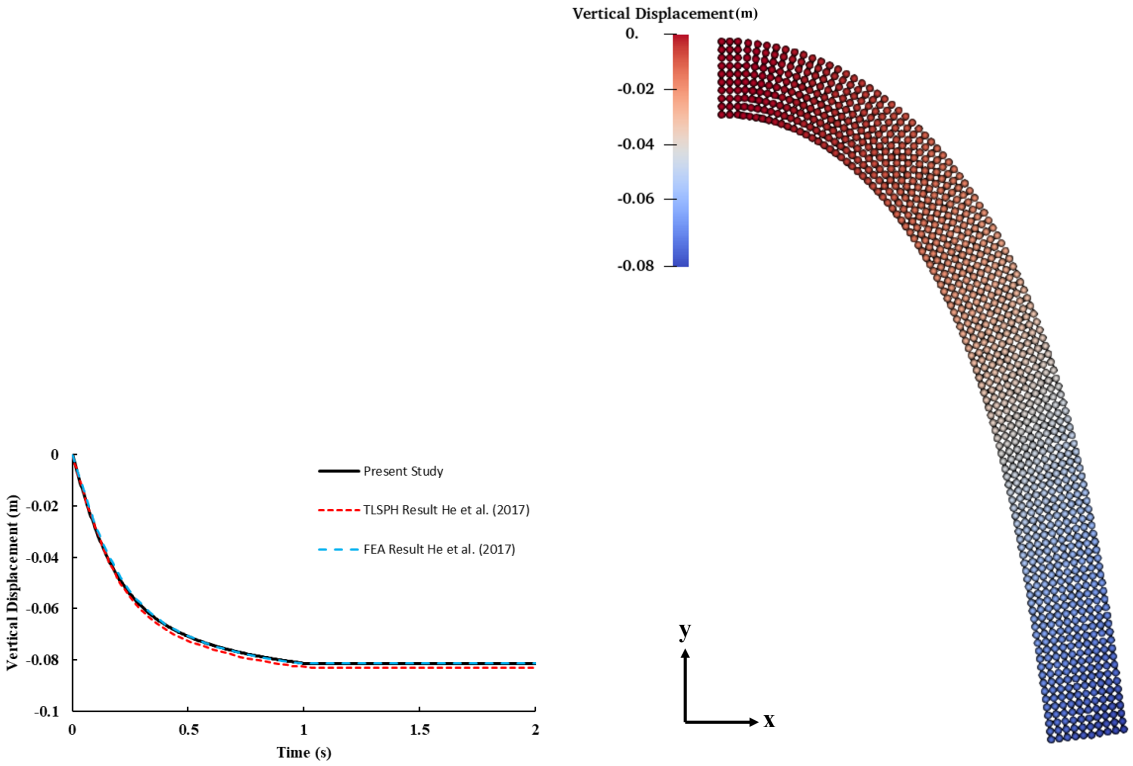

(a) Change of vertical displacement over time.

(b) 2D deformed beam at t = 2 s.

Figure 3.2 Simulation results of 2D cantilever beam.

the implemented stabilization techniques.

3.1.2 3D Cantilever Beam Simulation

The geometry of the 3D beam is presented in Figure 3.3. Analogous to the 2D case, a clamped boundary condition is imposed by fixing the first three layers of particles. The applied load is distributed across the surface of the beam tip, affecting 100 particles, which are visually indicated in black. This force increases linearly from t = 0 s to t = 0.5 s and subsequently remains constant until t = 1 s. Each particle's mass is defined as $\rho(\Delta x)^3$ and the corresponding external acceleration term, $b_i(t)$, is specified in Equation 3.3, where N_b denotes the number of particles subjected to the external force.

$$b_i(t) = \begin{cases} \dfrac{17500t}{\rho(\Delta x)^3 N_b}, & t < 1.0\,\text{s}, \\ \dfrac{17500}{\rho(\Delta x)^3 N_b}, & 1.0 \leq t \leq 2.0\,\text{s}, \end{cases} \tag{3.2}$$

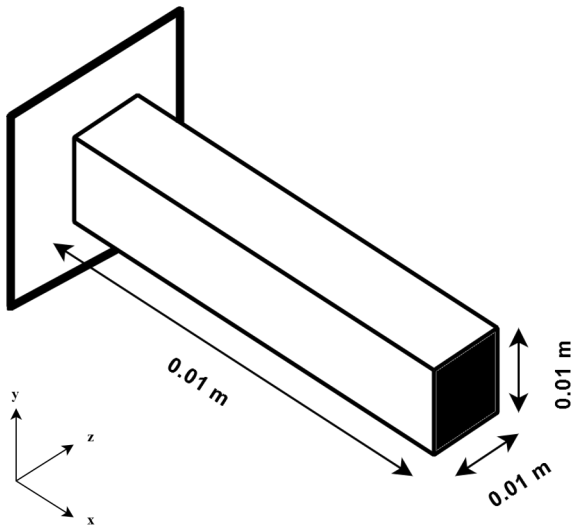

Figure 3.3 3D cantilever beam.

Figure 3.4a compares the vertical displacement of the beam tip over time with the results presented by He et al. (He & Lei, 2019). The corresponding displacement field of the beam at t = 1 s is shown in Figure 3.4b. Notably, the displacement reaches a plateau at t=0.5 s and remains constant until the simulation concludes at t = 1 s. While He et al. (He & Lei, 2019) provide results up to the steady-state (i.e., t = 0.5 s), our study extends the displacement time history beyond this point to demonstrate the sustained stability of the simulation. As Figure 3.4a clearly illustrates, our results exhibit strong agreement with the existing literature, confirming that our TLSPH solver effectively captures the large deformation behavior of elastic materials in both 2D and 3D with high accuracy.

3.2 A Novel TLSPH Approach for Modeling Damage in Elastic Solids

Having successfully validated the in-house TLSPH code for undamaged structures in both 2D and 3D, we then integrated the proposed novel damage model. Initially, the well-known Kalthoff-Winkler crack propagation experiment is modeled in both 2D and 3D as a benchmark. Subsequently, the dynamic crack branching experiment, a recognized Mode-I opening scenario, is simulated and results of both cases are compared with existing literature.

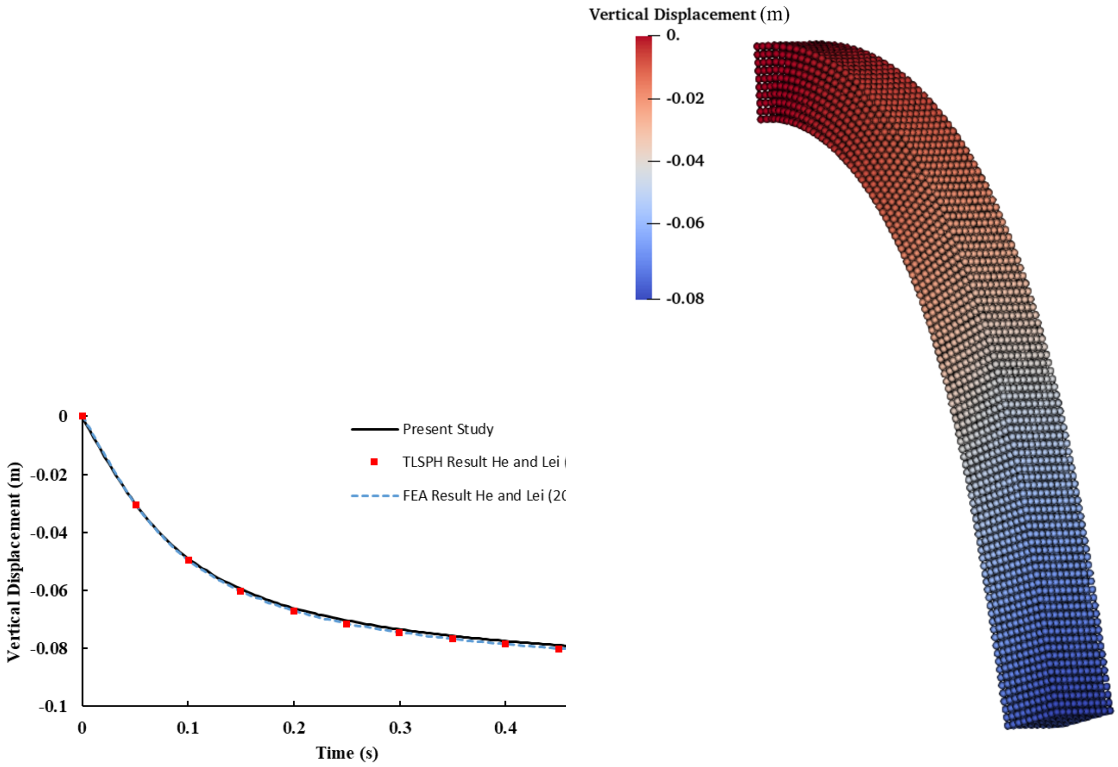

(a) Change of vertical displacement over time. (b) 3D deformed beam at t = 1 s.

Figure 3.4 Simulation results of 3D cantilever beam.

3.2.1 Kalthoff - Winkler Experiment

The novel TLSPH damage model presented in Section 2.3.1 is validated using 2D and 3D simulations of the dynamic Kalthoff-Winkler experiment, a common benchmark problem for crack propagation. This experiment investigates crack propagation behavior initiated by the in-plane impact of an object, traveling at a velocity of v_0 onto the top edge of a plate. The impact occurs between two pre-existing cracks as shown 2D and 3D illustrations in Figure 3.5 and Figure 3.6, respectively. The particles on the impact surface are given velocity boundary condition which develops from 0 to v_0 in 1 μs then remains constant. The material properties are given in Table 3.2. As common coefficients for both 2D and 3D models:

- Δx and hourglass correction coefficient γ are set to 0.001 m and 0, respectively.
- The velocity smoothing is performed by setting ϕ_c and ϵ as 0.65 and 0.1 after numerical trials.

Table 3.2 Material properties for the Kalthoff-Winkler experiment.

Parameter	**Young's Modulus**	**Density**	**Poisson Ratio**	$\mathbf{G_c}$
Value	190 GPa	8000 kg/m^3	0.3	22.13 kJ/m^2

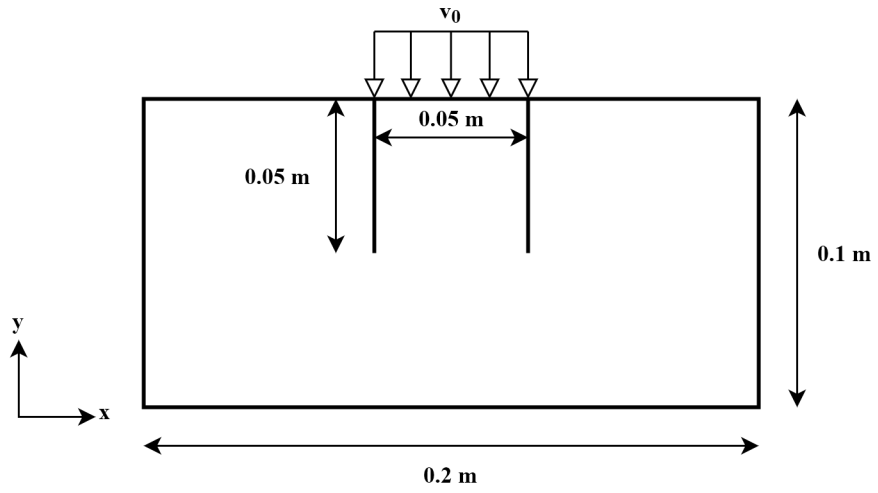

Figure 3.5 Set-up for 2D Kalthoff-Winkler experiment.

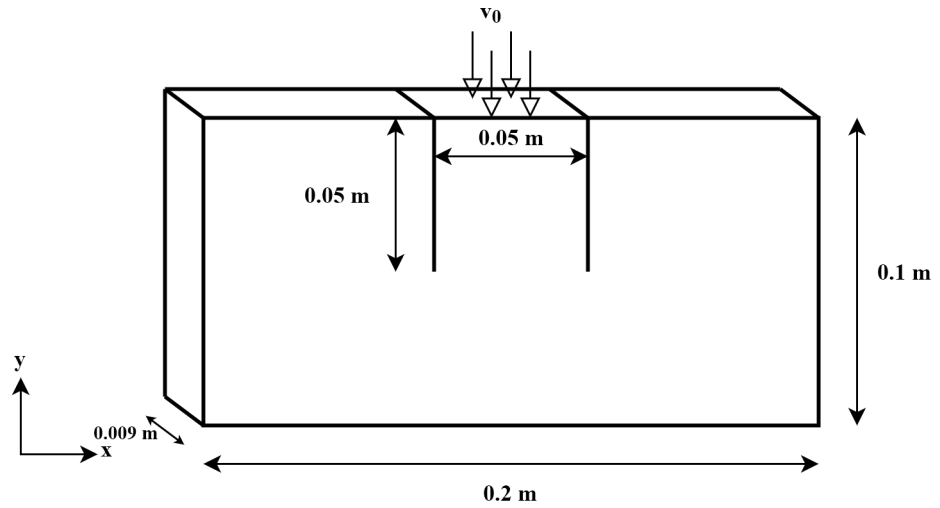

Figure 3.6 Set-up for 3D Kalthoff-Winkler experiment.

3.2.1.1 2D Kalthoff - Winkler experiment

Figure 3.5 depicts the 2D plate for Kalthoff - Winkler experiment. After several runs of simulations, the artificial viscosity coefficients α_0, α_d and β are determined as 0.09, 3.1 and 0, respectively. On the other hand, the critical stretch s_c is 0.01 m and the model consists total number of 20300 particle with time step of 10^-9 s. To be able to compare the results with the literature, the most common impact velocity 16.5 m/s is set as v_0.

Before obtaining the final simulation results, a convergence study is performed for the optimum particle spacing. To this end, different simulations are run with different particle spacings of 1.67 mm, 1.33 mm, 1.11 mm and 1.0 mm and their corresponding crack propagation angle and total simulation time for cracks reaching the side edges are considered as criteria. Table 3.3 provides crack propagation angles from various studies, obtained with different methods. Convergence study results

Table 3.3 Reported crack propagation angles for Kalthoff-Winkler experiment.

Study	**Method**	**Reported Angle**
Kalthoff (Kalthoff & Winkler, 1988)	Original Experiment	$\approx 70°$
Belytschko et al. (Belytschko, Chen, Xu & Zi, 2003)	XFEM	$\approx 58°$
Braun et al. (Braun & Fernández-Sáez, 2014)	2D Discrete Model	$\approx 65° - 70°$
Zhou et al. (Zhou, Wang & Qian, 2016)	Peridynamics	$\approx 65° - 70°$
Islam and Peng (Islam & Peng, 2019)	TLSPH	$\approx 77°$

for each resolution is as below:

- Δx = 1.67 mm 52°
- Δx = 1.33 mm 69°
- Δx = 1.11 mm 66°
- Δx = 1.0 mm 68°

For the case of Δx = 1.67 mm, the crack propagation starts at t = 30 μs and the crack reaches the lower edge of the plate at t = 110 μs. In the original experiment, the crack propagates diagonally and reaches the side lefts and not the lower edge. Thus, this resolution gives the worst result. In the case with Δx = 1.33 mm, crack

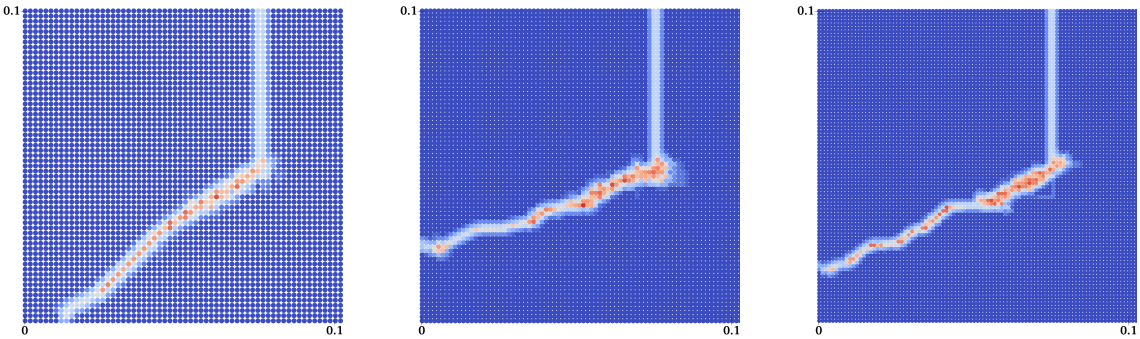

(a) $\Delta x = 1.67$ mm (b) $\Delta x = 1.33$ mm (c) $\Delta x = 1.11$ mm

Figure 3.7 The crack propagation paths for different resolutions.

starts to propagate at t = 26 μs and reaches the side edge of the plate at t = 114 μs. Furthermore, for Δx = 1.11 mm and Δx = 1.0 mm, initiation of the crack propagation occurs at t = 26 μs and t = 24 μs while the simulation is completed at t = 102 μs and t = 98 μs, respectively. When considering the simulation time varies between 80 μs and 90 μs and the crack propagation angle $\approx 70^\circ$ in the literature, the best result is considered as Δx = 1.0 mm. Figure 3.7 illustrates the crack propagation paths for Δx = 1.67 mm, Δx = 1.33 mm and Δx = 1.11 mm while Figure 3.8 shows for Δx = 1.0 mm. Figure 3.9 presents the crack propagation velocity for each resolution, alongside the Rayleigh wave speed, which represents the theoretical upper limit for crack propagation within a homogeneous, isotropic elastic body. Figure

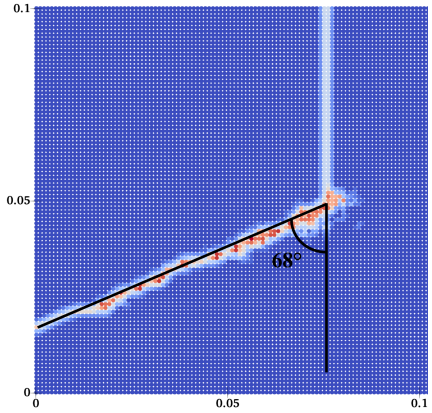

Figure 3.8 Crack propagation angle for $\Delta x = 1.0$ mm

3.10 shows the progression of crack propagation across several time of the simulation. As previously noted, crack initiation occurs at $t = 24, \mu$s. Following this, a diagonal crack path extending towards the plate's edges is observed, which is consistent with Kalthoff's original experimental findings (Kalthoff & Winkler, 1988). By $t = 98, \mu$s, both cracks have reached the boundaries of the plate, and the overall symmetry of the simulation is maintained. The crack propagation velocity is computed and compared

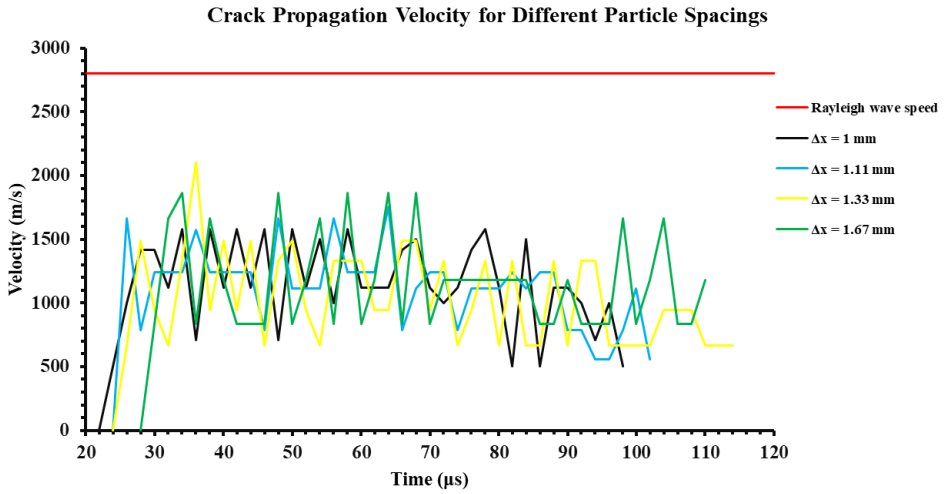

Figure 3.9 Crack propagation velocity for different particle spacings.

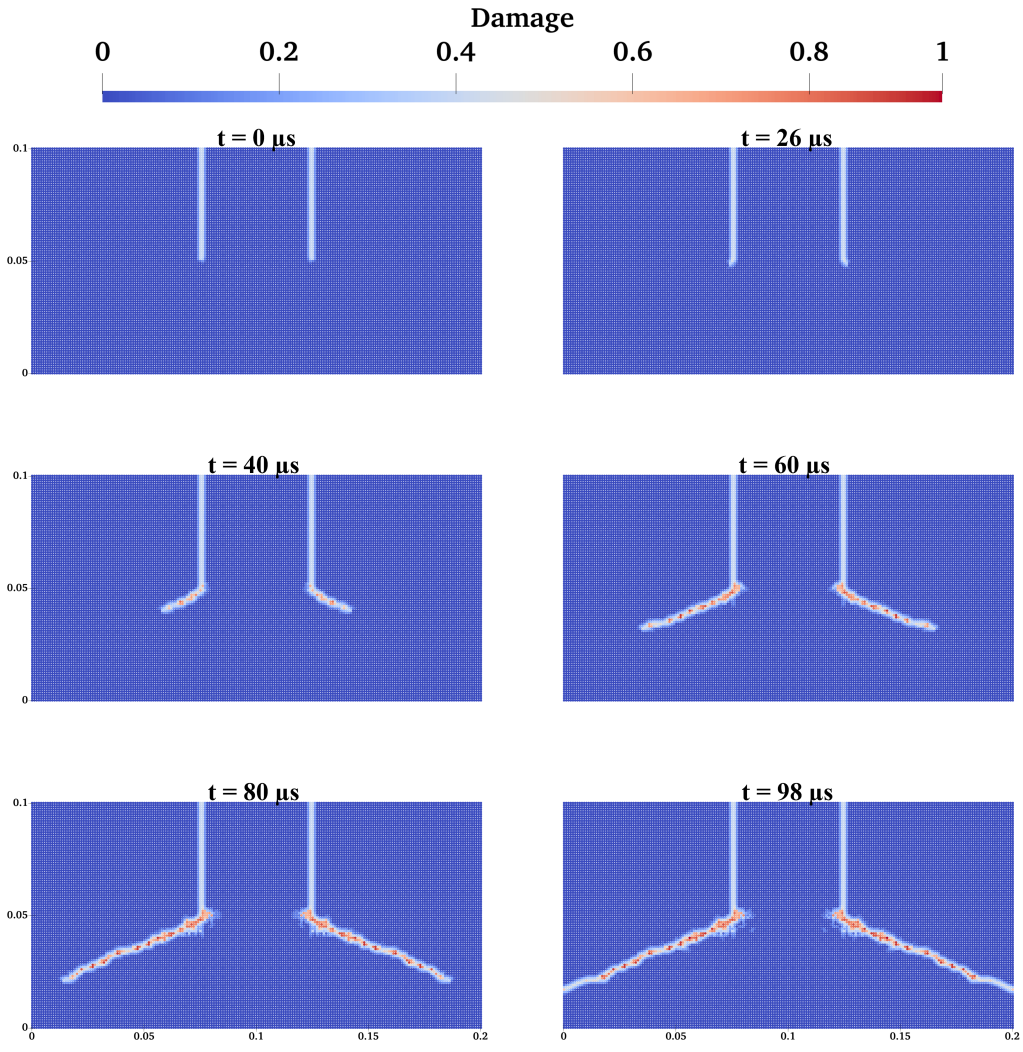

Figure 3.10 Crack propagation in Kalthoff-Winkler experiment.

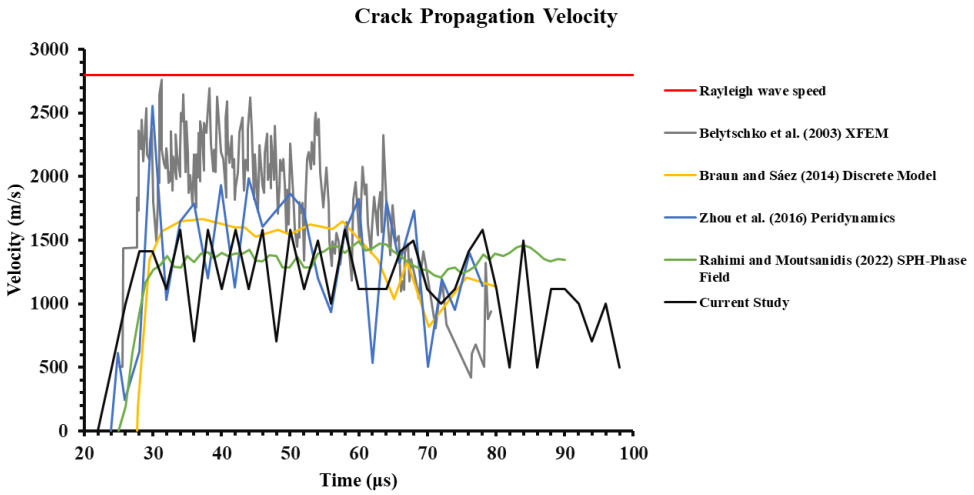

Figure 3.11 Crack propagation velocity in Kalthoff-Winkler simulation.

against results from other studies employing various numerical methods (Belytschko, Chen, Xu & Zi, 2003; Braun & Fernández-Sáez, 2014; Rahimi & Moutsanidis, 2022; Zhou, Wang & Qian, 2016). As depicted in Figure 3.11, the simulation results of the current study exhibit good agreement with the literature in terms of average crack propagation behavior. Specifically, the crack propagation velocity reached a peak of 1581 m/s, which corresponds to 56.46% of the Rayleigh wave speed (2800 m/s). This velocity is significant as the Rayleigh wave speed represents the theoretical maximum velocity a crack can achieve in a homogeneous, isotropic elastic material before typically experiencing crack branching (Ravi-Chandar, 1998). Based on these comparisons, it is evident that the findings of this study align well with both the original experimental observations and subsequent research in the field.

3.2.1.2 3D Kalthoff - Winkler experiment

For the 3D simulation, an impact velocity v_0 of -30 m/s is applied. The damage model coefficients, α_0 and α_d, are set to 0.2 and 4.5, respectively, with a critical stretch (s_c) of 0.085 m. The time step size is fixed at 10^{-8} s. Figure 3.6 illustrates the plate geometry, which is discretized into a total of 203000 particles. Crack initiation starts at t = 14μs, and the simulation concluded at t = 76μs when both cracks reached the left and right boundaries of the plate.

Initially, the crack propagates diagonally at an angle of 65°, which increased to 70° as the simulation progressed. Figure 3.12 displays the crack path on the plate at t = 76μs, shown from both isometric and x-y plane views. Additionally, the maximum

crack propagation velocity is computed to be 2236 m/s, remaining below the theoretical Rayleigh wave speed of 2799 m/s, as depicted in Figure 3.13. The numerical

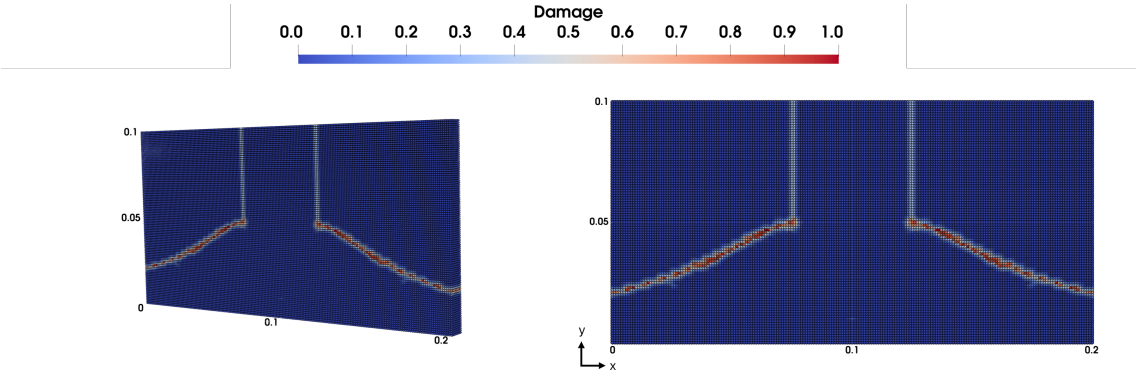

Figure 3.12 Crack path at t = 76 μs. Isometric view (left) and x-y plane (right).

findings of the current study are compared against three existing investigations, as summarized in Table 3.4. Raymond et al. (Raymond, Lemiale, Ibrahim & Lau, 2014) employed an updated Lagrangian SPH method, utilizing 330000 particles and a slightly different material density of 7830 kg/m^3. While they reported a crack propagation angle of 69.8°, specific details regarding the onset time of crack propagation and the total simulation duration are not provided. Their study presented the crack propagation velocity as a singular average value of 1200m/s, rather than illustrating its evolution over time. Ren et al. (Ren, Zhuang, Anitescu & Rabczuk, 2019) utilized the phase field method for their simulations on a plate with a thickness of 0.002 m. They explored various impact velocities, including 16.5m/s, 25m/s, and 40m/s, using a mesh comprising 406020 nodes and 1863670 elements. For the 25 m/s impact velocity case, which most closely resembles the conditions of the current study, crack propagation is observed to initiate at t=12.7 μs. However, their study did not provide corresponding crack propagation angle or velocity values for this specific impact scenario. Partmann et al. (Partmann, Wieners & Weinberg, 2023) conducted their analysis using the peridynamics method, reporting a crack propagation angle of 64°. Similar to some other studies, they did not provide information regarding crack propagation velocity. By comparing these established results from the literature, the current study's ability to accurately capture the complex 3D crack behavior in the Kalthoff-Winkler experiment is affirmed, demonstrating good alignment with existing research.

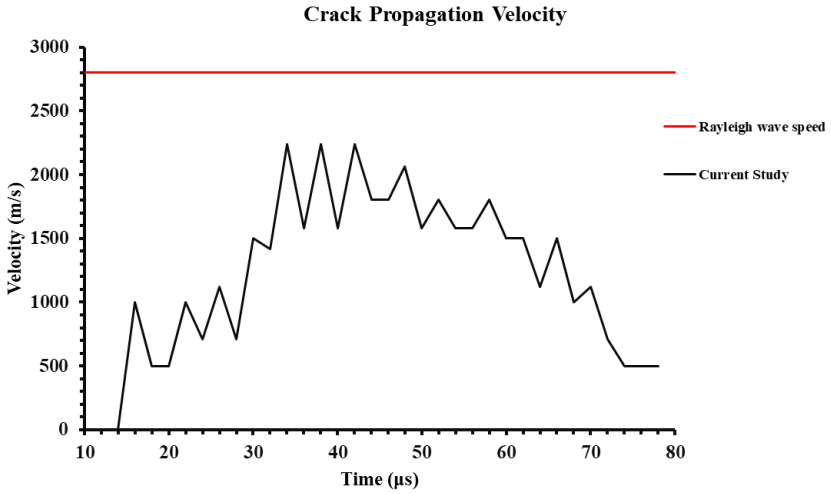

Figure 3.13 Crack propagation velocity for 3D Kalthoff-Winkler simulation.

Table 3.4 Results from the literature for 3D simulation of Kalthoff-Winkler.

	Impact Velocity	**Onset of Crack Propagation**	**Crack Propagation Angle**	**Crack Propagation Velocity**	**Resolution**
Raymond et al. (2014)	30 m/s	-	69.8°	1200 m/s (average)	330000 particles
Ren et al. (2019)	25 m/s	12.7 μs	-	-	406020 nodes
Partmann et al. (2023)	33 m/s	-	64°	-	124608
Current study	30 m/s	14 μs	65° - 70°	2236 m/s (maximum)	203000 particles

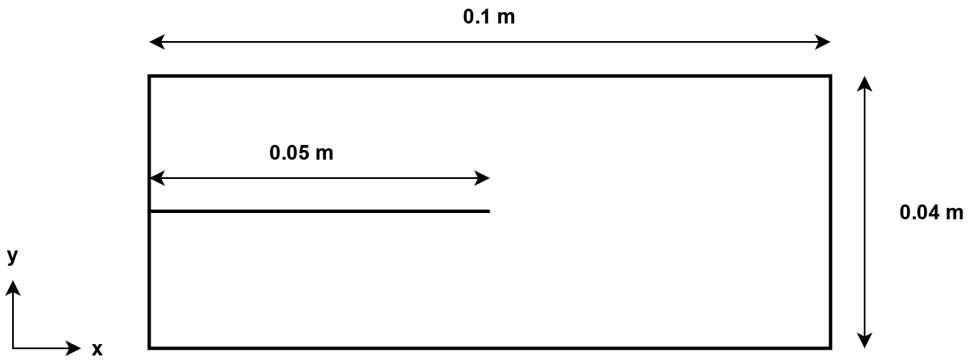

Figure 3.14 Geometry for dynamic crack branching simulation.

3.2.2 Dynamic Crack Branching

To further extend the investigation into crack propagation, a dynamic crack branching problem under Mode-I loading is simulated. The problem involves a plate with a pre-existing crack which is subjected to traction at both upper and lower edges. The initial geometry of this plate is presented in Figure 3.14. The material properties utilized in this simulation are detailed in Table 3.5. For the numerical discretization, a particle spacing Δx of $3.33x10^{-4}$ m is adopted which results in a total of 36,000 particles. The coefficients for artificial viscosity,α_0, α_d and β are set to 0.03, 0.4, and 0, respectively. For velocity smoothing, both ϕ_c and ϵ are determined to be 0.5 and the critical stretch, s_c is calculated as 5.3 x 10^-4 m. A uniform stress boundary condition (σ_0) of 1 MPa is applied to the top and bottom edges of the plate. It is important to note that applying stress boundary condition in SPH is not straightforward so the technique proposed by Douillet-Grellier et al. (Douillet-Grellier, Pramanik, Pan, Albaiz, Jones & Williams, 2017) is adopted. The initial

Table 3.5 Material properties for the crack branching simulation.

Parameter	**Young's Modulus**	**Density**	**Poisson Ratio**	**G_c**
Value	32 GPa	2450 kg/m^3	0.2	3 J/m^2

crack began to propagate at approximately t = 8 μs. subsequently splitting into two primary branches around t = 33 μs. Figure 3.15 illustrates the evolution of this crack, demonstrating that the characteristic crack paths were successfully captured when compared to findings from various literature sources (Belytschko, Chen, Xu & Zi, 2003; Borden, Verhoosel, Scott, Hughes & Landis, 2012; Li, Ning & Liu, 2022; Song, Areias & Belytschko, 2006; Xu, Liu, Liu, Zeng & Zhuang, 2014). Figure 3.16 presents the crack propagation velocity alongside results from other studies (Belytschko, Chen, Xu & Zi, 2003; Borden, Verhoosel, Scott, Hughes & Landis,

2012; Li, Ning & Liu, 2022; Song, Areias & Belytschko, 2006; Xu, Liu, Liu, Zeng & Zhuang, 2014). Our study's onset times for both crack propagation and branching are notably similar to those reported by the phase field method (Borden, Verhoosel, Scott, Hughes & Landis, 2012). However, it is observed that the phase field method tends to underestimate crack propagation velocity compared to other numerical approaches.The simulation concluded at t = 56 μs when both crack branches reached the right edge of the plate. Throughout the simulation, no inconsistent additional branches were observed, aligning closely with reported results. Furthermore, the crack propagation velocity remained below the Rayleigh wave speed (2163m/s), as anticipated.

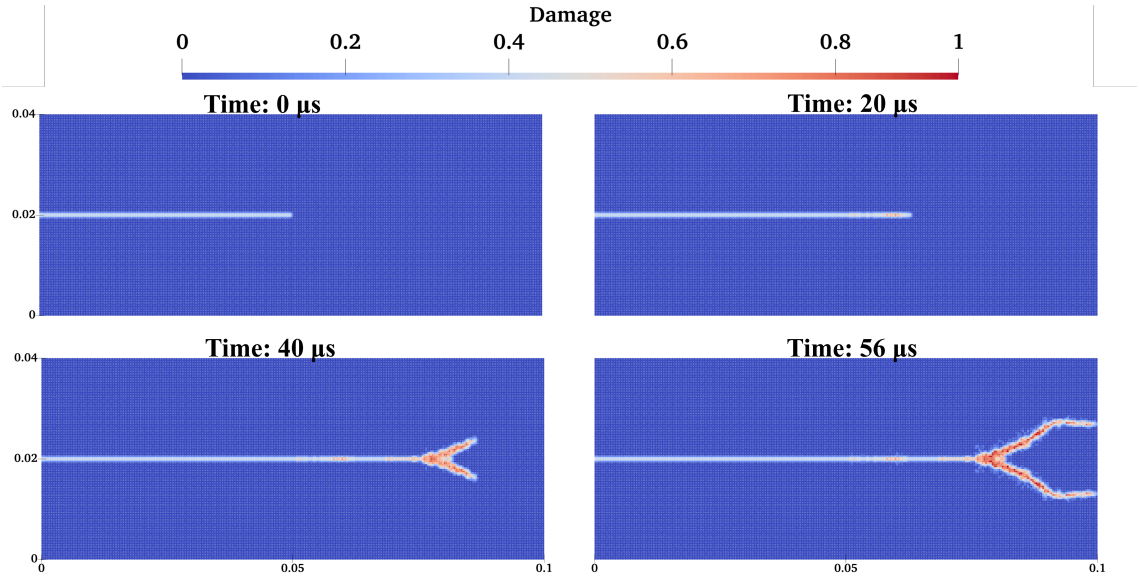

Figure 3.15 Evolution of dynamic crack branching.

3.3 A TLSPH Scheme for Deformation of the Composite Structures

To evaluate the deformation behavior of composite structures, we conducted dynamic simulations over a 0.5 second interval. This involved two different 3D two-layered composite beams, each with a unique ply orientation, and a two-layered composite plate. As no analytical solutions or existing literature results are available for these specific scenarios, we validated our TLSPH models by comparing their outcomes against results derived from our FEM models.

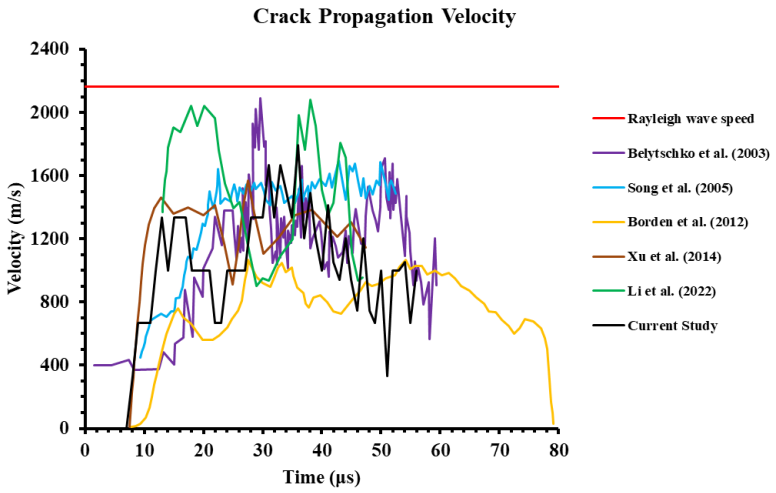

Figure 3.16 Crack propagation velocity in dynamic crack branching experiment.

3.3.1 Deformation of Composite Beams

This study examines the flexural response of a bi-layered composite beam, as illustrated in Figure 3.17, considering various fiber orientations in its individual layers. Fiber angles are defined with respect to the x-axis, which aligns with the beam's length. The y-axis represents the depth, and the z-axis denotes the thickness direction. The edge dimensions of the beam are $h = b = 0.01$ m and its length is $L = 0.1$ m with each layer is 0.005 m thick. Both layers are composed of carbon fiber-reinforced epoxy, with their material properties detailed in Table 3.6. Two different lay-up configurations are investigated: (1) a cross-ply laminate ([0°/90°]) and (2) an angle-ply laminate ([0°/45°]) in which the bottom layer's fibers are oriented at 0°, while the top layer's fibers are oriented at either 90°or 45°, depending on the case. For numerical discretization, the inter-particle distance, Δx, is set to 0.001 m and the smoothing length (h) is taken as $1.33\Delta x$. The time step size, Δt is determined by calculating Courant-Friedrichs-Lewy condition $0.2min\left(0.8\left(h/c_0\right), 0.25\sqrt{h/9.81}\right)$ and the artificial viscosity coefficients, α_i and β_i are taken as 0.3 and 0, respectively. The hourglass force coefficients, γ, is -85 and -90 for cross-ply and angle-ply beams, respectively. The material properties,carbon fiber reinforced epoxy, are given in Table 3.6. A temporal body force $b_i^z(t)$ of -1000 N per unit mass (kg), is applied to the central particle of the beam's cross-section according to the below time-dependent condition:

$$b_i^z(t) = \frac{-1000t}{\rho(\Delta x)^3}, \tag{3.3}$$

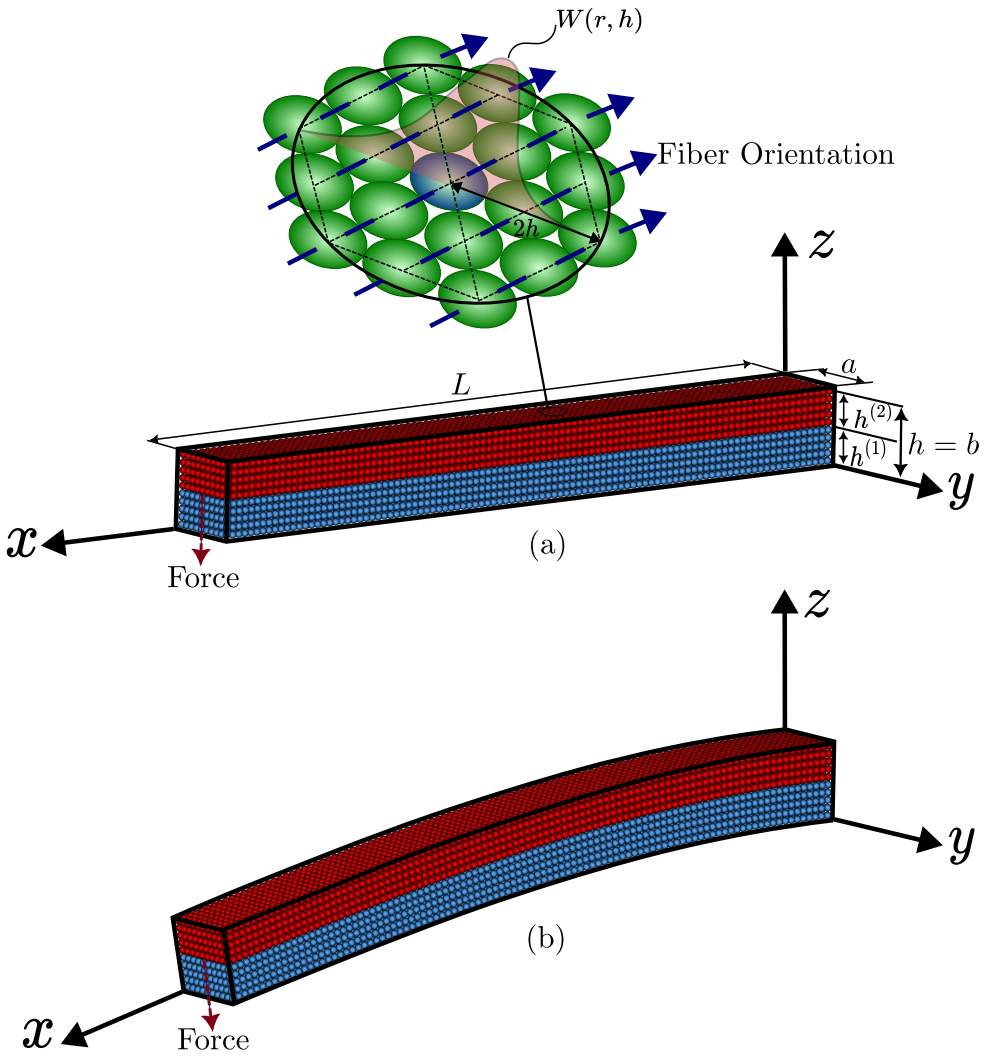

Figure 3.17 (a) Undeformed and (b) deformed beam.

Figure 3.18 and Figure 3.19 present a comparative displacement analysis between the TLSPH and FEM results for both the cross-ply and angle-ply beams. Figures 3.18a and 3.19a show the change of u_1 displacement with time for the cross section of the beam tip ($x = L, y = 0.5b, z$) for each beam. The slope of u_1 does not change with time which is due to same material properties for each layer and bending-dominated response. Moreover, there are no slope discontinuities observed since the shear effects are negligible. This consistent with the classical thin-beam theory where the bending behavior is much more compared to transverse shear behavior. The larger bending rotations occur for the cross-section as the simulation time increases with increasing load, which can be seen in figure as the slope of the lines are decreasing with time. The out of plane displacements u_3 of the beam-tip particle ($x = L, y = 0.5b, z = 0.5h$) of both approaches show a very close agreement, as Figures 3.18b and 3.19b demonstrate. This compatibility proves the capability of the proposed approach in flexural behavior for composite beams. The linearly increasing tip-load is responsible for the linear change of u_3 within time. Moreover, staying in the elastic

Table 3.6 Material properties for the composite beam.

Parameter	Value	Unit
E_1	121	GPa
E_2	8.6	GPa
E_3	8.6	GPa
G_{12}	4.7	GPa
G_{13}	4.7	GPa
G_{23}	3.1	GPa
ν_{12}	0.27	-
ν_{13}	0.27	-
ν_{23}	0.4	-
ρ	1490	kg/m^3

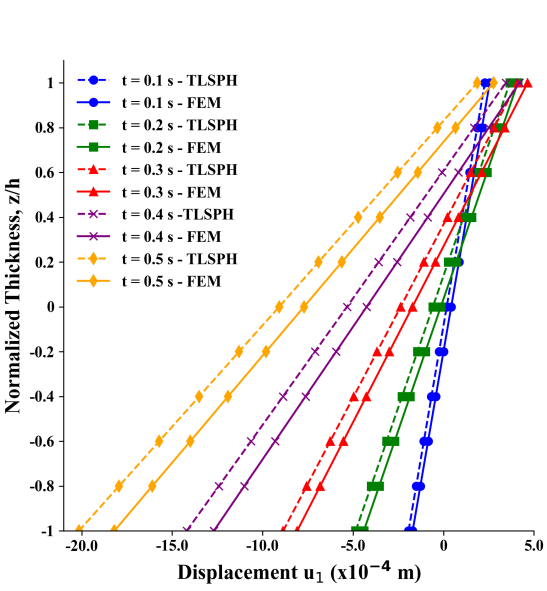

(a) Change of u_1 with time.

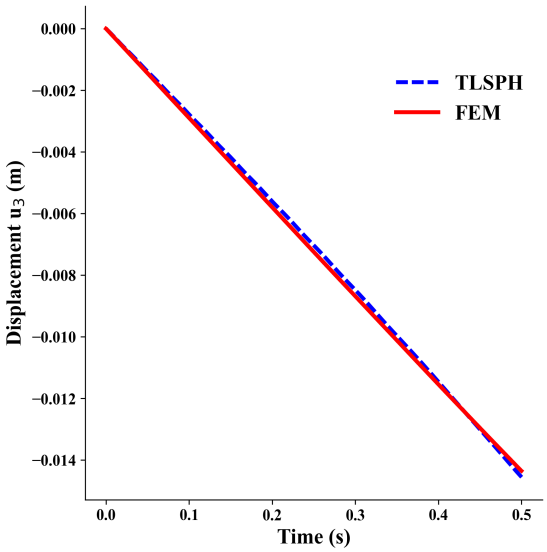

(b) Change of u_3 the beam-tip particle with time.

Figure 3.18 Comparison of results for the 0°/90° fiber configuration.

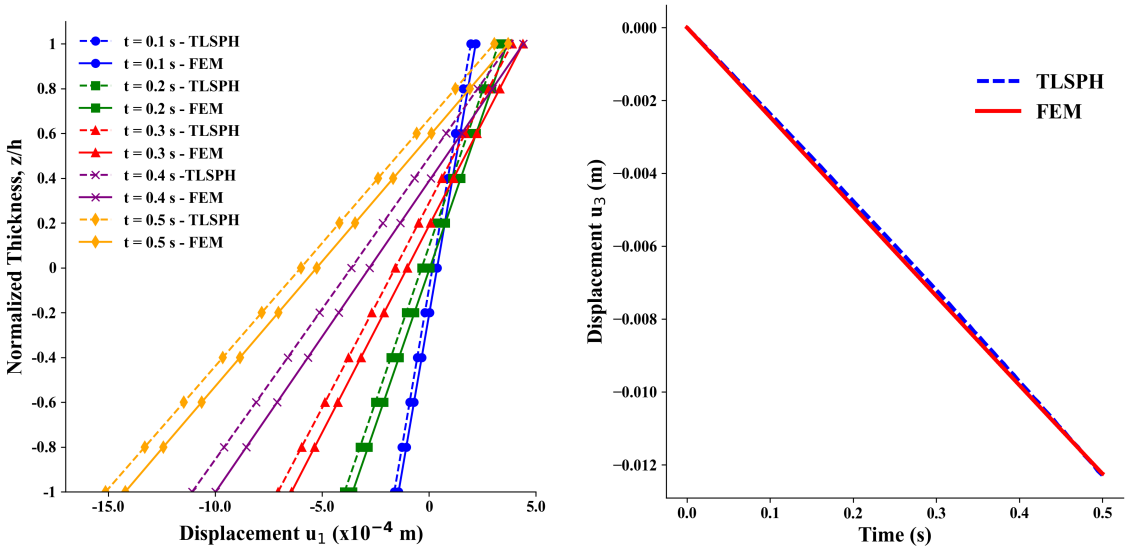

(a) Change of the cross-sectional u-displacement with time.

(b) Change of the z displacement of beam-tip particle with time.

Figure 3.19 Comparison of results for the 0°/45° fiber configuration.

regime, the small deformation and the absence of any geometric nonlinearities are also creates a linear temporal change of u_3. Thus, utilizing reduced transformed stiffness matrices are accurate and computationally efficient for layered composite beams.

3.3.2 Deformation of Composite Plate

To further validate the proposed method's capability, a two-layered composite plate with a cross-ply configuration ([0°/90°]) is modeled using both commercial FEM software and our in-house TLSPH code, following Algorithm 2. The dimensions of the square plate are $a = b = 0.1m$ while its thickness is $h = 0.004m$. The material used in previous case is also used for the plate. The undeformed and deformed states of the plate is given in Figure 3.20. A linearly increasing temporal body force of -10 N per kilogram is applied to each particle on the top surface of the plate in the TLSPH model, while an equivalent load per square meter (1 MPa) is applied to the top surface in the FEM model. The artificial viscosity coefficient α is 0.2 and the hourglass force coefficient is taken as -10 with the particle spacing of 0.001 m. To investigate the accuracy of proposed method, the displacement components u_1, u_2 and u_3 are compared at t = 0.1, 0.2, 0.3, 0.4 and 0.5 seconds. The outputs are recorded for upper surface (i.e., the surface that has 90°oriented fibers) and they are

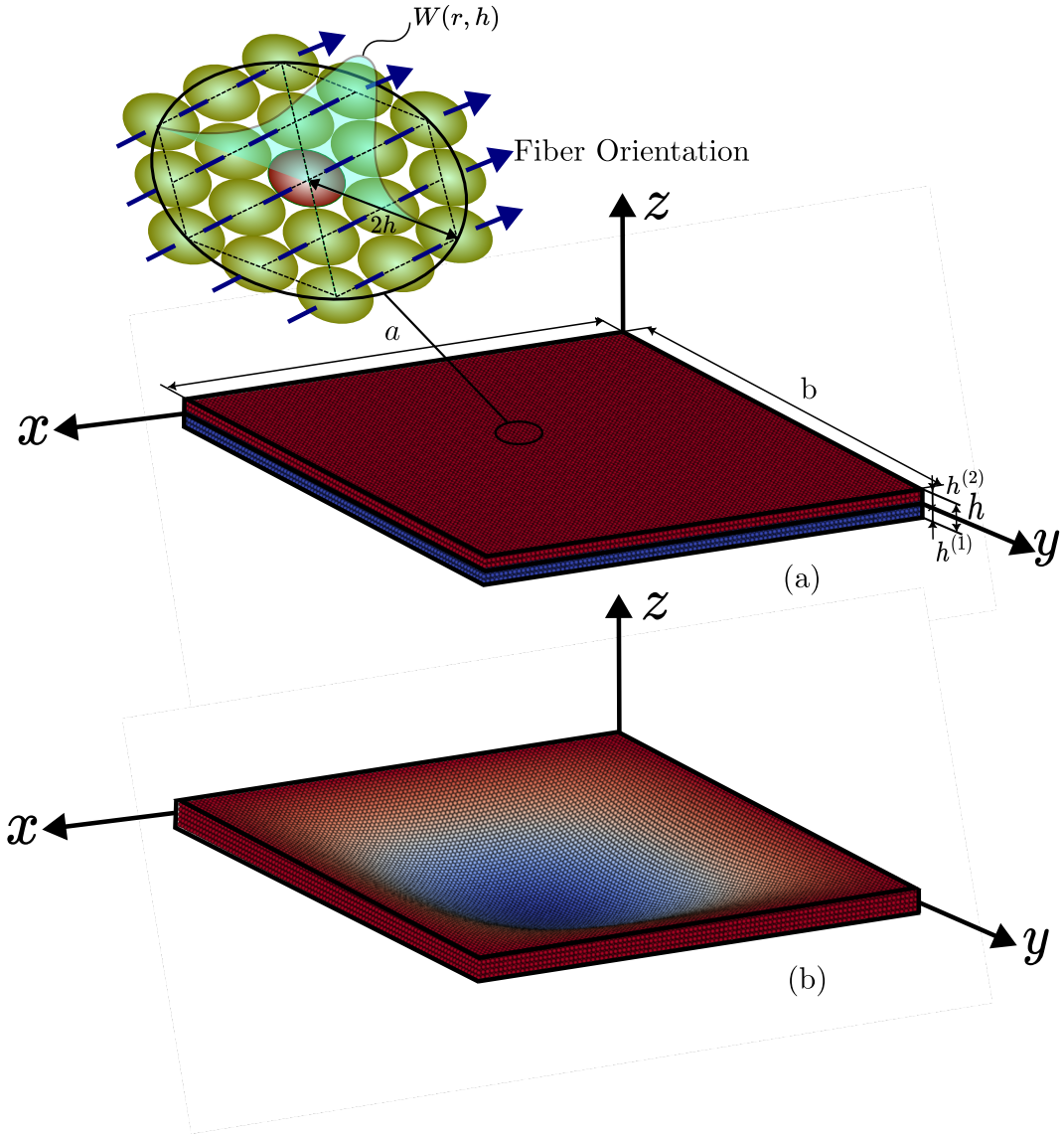

Figure 3.20 (a) Undeformed and (b) deformed plate.

compared with the FEM model, as depicted in Figure 3.23 and Table 3.7.

In Figure 3.23, the contour of the u_1, u_2 and u_3 displacement component is given for $t = 0.5s$. As it can be seen in Figure 3.23a and Figure 3.23b, the in-plane displacement components u_1 and u_2 in both methods are in a strong agreement and they show a symmetry which characterizes the bending response. This symmetry can be attributed to the equal distribution of the loading and fully-clamped boundary constraints of the edges. For TLSPH, u_1 and u_2 displacements are $\pm 3.252 \times 10^{-4}$ m and $\pm 3.838 \times 10^{-4}$ respectively while these values are predicted slightly higher in FEM as $\pm 3.521 \times 10^{-4}$ and $\pm 4.02 \times 10^{-4}$. In both approaches, the maximum deformation values are seen at the center of the plate where the bending curvature is the highest. As expected, the out of plane displacement u_3 is much higher than the in-plane components since the nature of the loading is out of plane.

Table 3.7 Comparison of TLSPH and FEM Model Results for Displacement Components

Time (s)	Model	u_1 ($x10^{-4}$ m)		u_2 ($x10^{-4}$ m)		u_3 ($x10^{-4}$ m)	
		Max	Min	Max	Min	Max	Min
0.1	TLSPH	1.084	−1.084	1.259	−1.259	0	−14.15
	FEM	1.447	-1.447	1.501	-1.501	0	−17.24
0.2	TLSPH	1.848	−1.848	2.181	−2.181	0	−24.45
	FEM	2.248	-2.248	2.401	-2.401	0	−26.85
0.3	TLSPH	2.420	−2.420	2.867	−2.867	0	−32.43
	FEM	2.784	-2.784	3.040	-3.040	0	−33.34
0.4	TLSPH	2.842	−2.842	3.456	−3.456	0	−38.43
	FEM	3.195	-3.195	3.563	-3.563	0	−38.34
0.5	TLSPH	3.252	−3.252	3.838	−3.838	0	−44.14
	FEM	3.521	−3.521	4.027	−4.014	0	−42.45

Table 3.8 Effect of various hourglass coefficients on the accuracy of displacement components

Hourglass Coefficient	u_1 ($\times10^{-4}$ m)			u_2 ($\times10^{-4}$ m)			u_3 ($\times10^{-4}$ m)	
	Max	Min	Error	Max	Min	Error	Min	Error
−10	3.252	−3.252	7.64%	3.838	−3.838	4.69%	−44.14	3.98%
−15	3.122	−3.122	11.33%	3.750	−3.750	6.88%	−42.96	1.20%
−20	3.076	−3.076	12.63%	3.697	−3.697	8.19%	−42.58	0.30%
−25	3.035	−3.035	13.80%	3.647	−3.647	9.43%	−42.34	0.26%

To analyze the effect of the hourglass coefficient γ on the predicted displacement components in TLSPH method, several simulations are run with different γ values and the results are reported in Table 3.8. The results shows that the change of γ value has different effects on different displacement components. For instance, increasing γ lowers the error percentage of u_3 from 3.98% to 0.26%. On the other hand, it grows the error percentage of u_1 from 7.64% to 13.80% and u_2 from 4.69% to 9.43%. This contrast in the trend of the error percentages with changing γ values shows that an optimization is necessary since a single γ for one of the displacement component does not mean an improvement for the whole solution field. To the best of the author's knowledge, this behavior may be due to the dependency of the total system energy to the all displacement components. Therefore, to ensure a robust global minimum of the hourglass energy's contribution to the total system energy, it's essential to balance hourglass stabilization across the entire displacement field, rather than optimizing for a single component. In this study, the hourglass coefficients are determined through a trial-and-error monitoring procedure. In future studies, systematic optimization methods may be developed to obtain more robust γ calculation schemes for various material models.

Figure 3.21a and Figure 3.21b illustrate the temporal variation of the in-plane displacements u_1 and u_2 and the out-of-plane deflection u_3, respectively. These displacements are measured at a point on the top surface with coordinates $x = y = 0.075m$. Since the fiber orientations of the two layers are different from each other, an anisotropic stiffness is formed and this is what the observed displacement behavior is governed by. The bottom layer's 0°oriented fibers creates a resistance agains the deformation along the x-axis and the top layer's 90°oriented fibers provides a stiffness along the y-axis. A bending-dominated behavior is expected due to the clamped edges under a uniform out-of-plane pressure to the upper surface. Thus, u_3 is much higher than u_1 and u_2, whose value is mainly depends on the effective bending stiffness of the orthotropic laminate, the loading and the boundary conditions. As the graphs show, the proposed TLSPH approach and FEM results are in a good agreement especially their $u3$ predictions. As in the cases of u_1 and u_2, these two approaches generates modestly different values through time for both beam and plate simulation scenarios as illustrated in Figure 3.18a, Figure 3.19a, Figure 3.23a, Figure 3.23b and Figure 3.21a. This discrepancy stems from artificial viscosity and hourglass control forces that are the additional stabilization approaches used in the TLSPH. By incorporating these mechanisms, the numerical instabilities are suppressed while a numerical damping is introduced to the system. As far as the authors are aware, as a result of this damping, sharp local changes are inherently inhibited and the displacement amplitudes are altered. Furthermore, the type of

the main equations that are solved by FEM and TLSPH are different from each other. In FEM, an integration that consists of shape functions and Gauss points is performed to solve the the weak form of the conservation of the linear momentum. On the other hand, in TLSPH, a kernel interpolation in a meshless context is used to solve the strong form of the conservation equation. These differences reveals a significant trade-off: FEM offers precise kinematic fidelity, whereas TLSPH provides mesh-free computational flexibility and adaptability. Figure 3.22 presents a com-

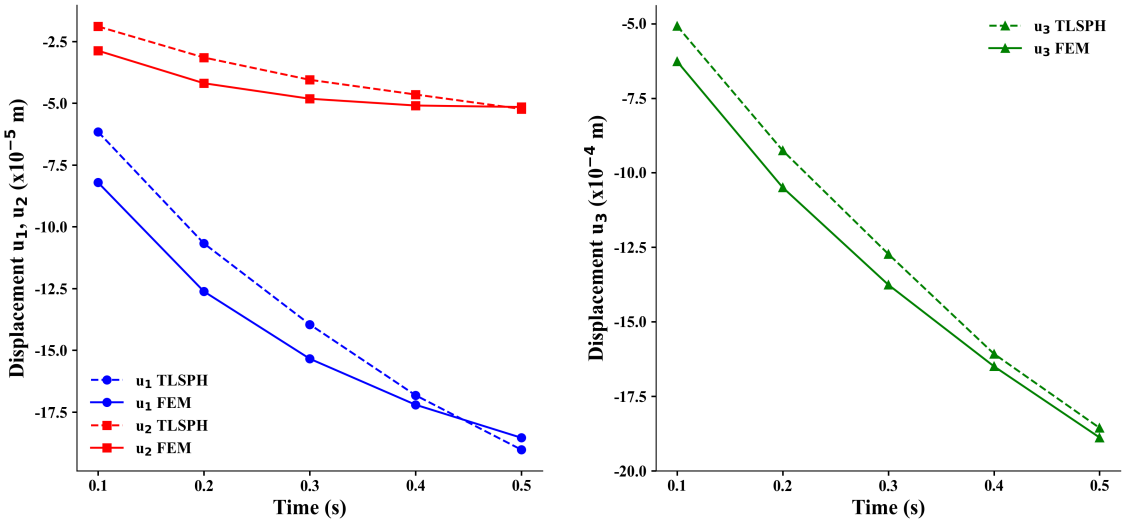

(a) Change of the in-plane displacements with time for upper-right middle point of the composite plate.

(b) Change of the u_3 displacement with time for upper-right middle point of the composite plate.

Figure 3.21 Comparison of displacement components for the composite plate.

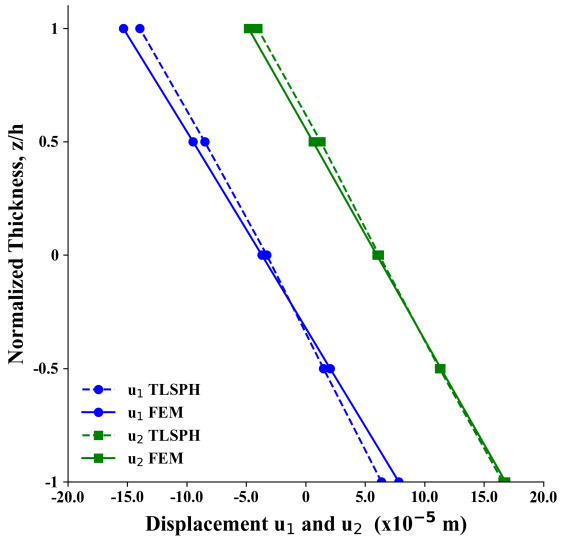

Figure 3.22 Change of the in-plane displacements through the thickness for point A($x = y = 0.075m$).

parative analysis of in-plane displacement variations across the plate's thickness at

point A. The displacements show an approximately linear distribution through the thickness, suggesting that the material transition between plies has a negligible impact on the laminate's deformation at this specific location. This behavior is likely due to the similar material properties of the two layers, which dominate the local response and outweigh the effect of differing fiber orientations under the applied flexural loading, similar to observations in the beam case.

As seen in the graph, at the reference neutral plane ($z/h = 0$) the in-plane displacements are found to be different than 0 which indicates a membrane response as a result of anti-symmetric fiber configuration. As the graph clearly illustrates, the magnitude of bending-induced displacement increases with distance from the neutral plane, toward the outer surfaces. This observation is consistent with classical bending theory. The close agreement between the TLSPH method and the reference 3D continuum FEM solution confirms that our proposed approach reliably captures the mechanical response of composite laminates reinforced by different fiber orientations.

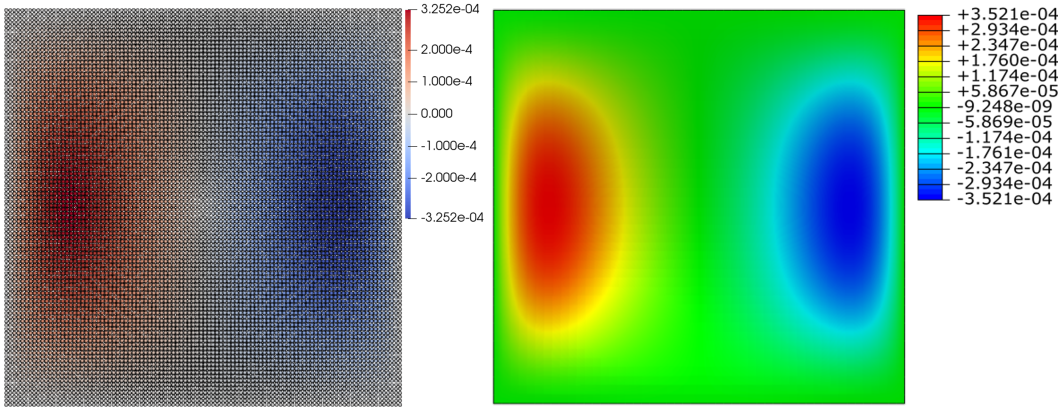

(a) Displacement u_1 for TLSPH (left) and FEM (right)

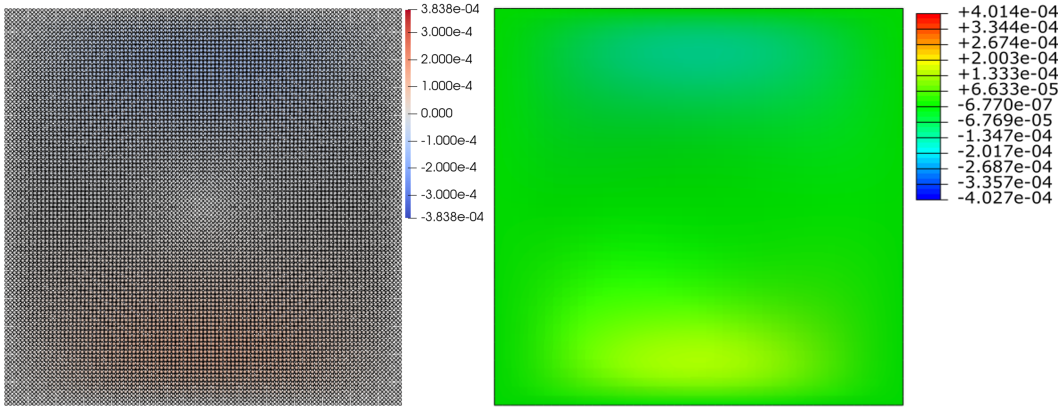

(b) Displacement u_2 for TLSPH (left) and FEM (right)

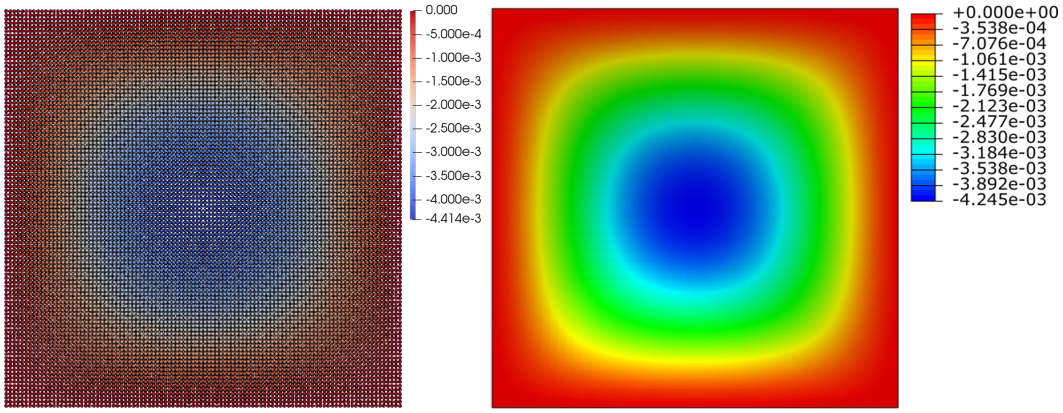

(c) Displacement u_3 for TLSPH (left) and FEM (right)

Figure 3.23 Comparison of deformations for TLSPH and FEM

4. CONCLUSION

This dissertation introduced a novel computational framework based on the TLSPH method to address key limitations in simulating fracture in elastic solids and the deformation of laminated composite structures. Two primary contributions were presented: (i) a TLSPH damage model for isotropic elastic media and (ii) a TLSPH macro-modeling approach for dynamic analysis of laminated composites.

In the first part, a TLSPH formulation was developed that incorporates a stretch-based failure criterion inspired by bond-based peridynamics. Inter-particle interactions were governed by a critical stretch value s_c, and particle bonds were eliminated once this threshold was exceeded. To counteract the numerical instabilities caused by such bond eliminationsuch as tensile instability, rank deficiency, and artificial clusteringseveral stabilization techniques were embedded into the numerical framework. These included:

- artificial viscosity formulation with a locally adaptive coefficient α_i based on the smoothed damage field ϕ_i',
- hourglass control forces f^{HG} inspired by FEM's zero-energy mode correction,
- velocity smoothing for damaged regions.

The in-house TLSPH code was initially validated by simulating the deformation of 2D and 3D isotropic elastic beams. Comparisons of the beam-tip displacement with existing literature studies revealed that the results were nearly identical.Then the in-house code was developed for a novel damage model. Accuracy and robustness of the proposed method were validated through benchmark fracture simulations, including the 2D/3D Kalthoff-Winkler experiment and dynamic crack branching. The model successfully captured critical fracture features such as propagation paths, crack branching, and tip velocities, demonstrating its capability to simulate complex fracture dynamics without remeshing.

The second part of the research extended the TLSPH formulation to 3D laminated composite structures (beams and plate) subjected to quasi-static loading. Unlike

mid-plane or layer-equivalent theories FSDT, the developed model discretized each ply through its thickness using multiple TLSPH particles, thereby enabling layer-specific displacement evaluation. The governing equations were solved in strong form with orthotropic constitutive relations transformed from local fiber-aligned axes to the global frame via the transformation matrix. To maintain numerical, the same stabilization mechanisms used in the damage model were applied. Moreover, simulations employed smooth ramp functions for load application to approximate quasi-static responses while preserving the time-dependent characteristics of the TLSPH scheme. Simulation results for 3D composite beams and plate confirmed the model's ability to:

- capture the temporal evolution of the beam-tip deformation for composite beams,
- capture the overall deformation pattern for the composite plate,
- account for fiber orientation and anisotropy effects without resorting to micro-scale modeling,
- remain stable under quasi-static loading conditions.

In conclusion, this dissertation contributes a consistent, unified, and efficient particle-based framework for solid mechanics simulations involving both fracture and laminated composites. The proposed TLSPH-based formulations overcome several longstanding limitations of traditional mesh-based and meshless methods, offering:

- a robust, easy-to-implement formulation framework
- mesh-independence and remeshing-free handling of crack propagation,
- physically-motivated stabilization techniques for improved numerical robustness,
- extensibility to anisotropic materials with minimal additional complexity.

The work presented herein provides a solid foundation for advancing TLSPH-based techniques in both academic research and practical engineering applications involving fracture and composite structures.

Conclusion

This dissertation presents a unified and robust particle-based computational framework for modeling two distinct yet practically critical classes of problems in solid mechanics: dynamic brittle fracture in isotropic media and quasi-static deformation in laminated composite structures. Using the Total Lagrangian Smoothed Particle Hydrodynamics (TLSPH) formulation, the proposed methodology eliminates the dependency on mesh connectivity, which often hinders the accuracy and efficiency of conventional finite element methods in high-gradient, discontinuous, or anisotropic scenarios.

In the first part of the thesis, a novel TLSPH damage model was developed for isotropic solids. This formulation adopts a stretch-based bond-breaking criterion inspired by peridynamic concepts, allowing for a physically motivated and mesh-free simulation of crack initiation and propagation. To address numerical instabilities arising from damage evolutionsuch as tensile instability and particle clusteringstabilization strategies including adaptive artificial viscosity, hourglass control forces, and velocity filtering were incorporated. Benchmark simulations, including dynamic crack branching and the KalthoffWinkler experiment in both two and three dimensions, verified the accuracy and robustness of the model in capturing complex fracture phenomena without requiring remeshing or enrichment.

In the second part of the thesis, the TLSPH framework was extended to simulate the large-deformation behavior of laminated composite beams and plates under quasi-static flexural loading. Each ply was discretized through the thickness using SPH particles, and orthotropic constitutive behavior was accurately modeled via tensor transformation techniques. The model's ability to capture essential laminate mechanicssuch as bendingstretching coupling, fiber-direction-dependent stiffness, and through-thickness displacement gradientswas validated through comparisons with high-fidelity three-dimensional FEM simulations. In particular, the formulation reproduced the characteristic linear distribution of in-plane displacements and parabolic deflection patterns in unsymmetric cross-ply laminates, confirming its physical fidelity. The influence of stabilization parameters, such as the hourglass coefficient, was also explored to balance numerical damping and accuracy.

This research is, to the best of the author's knowledge, the first comprehensive application of TLSPH to both crack modeling and the macro-scale deformation of layered composite structures in a single, consistent framework. The results demonstrate the flexibility and extensibility of the method for simulating a wide range of solid mechanics problems. Future directions include the integration of interlaminar damage and delamination models, rate-dependent material behavior, and real-world

validation through experimental comparisons.

Overall, the proposed TLSPH-based formulations offer a promising alternative to mesh-based methods by removing remeshing bottlenecks, handling complex material behavior with ease, and delivering high-fidelity results across multiple application domains in computational solid mechanics.

5. FUTURE STUDIES

Although this thesis presents a robust TLSPH framework capable of modeling brittle fracture and dynamic deformation in laminated composites, the potential of particle-based methods extends far beyond the current scope. Future developments may focus on enhancing material modeling capabilities, expanding the range of physical phenomena that can be captured, and improving computational efficiency. Such advancements would increase the versatility of the TLSPH approach and enable its application to more complex engineering systems and material behaviors.

Firstly, the current TLSPH damage model is limited to brittle failure, where material separation occurs without significant plastic deformation. However, many structural and engineering materials undergo extensive plastic yielding before fracture. Extending the current TLSPH framework to incorporate elasto-plastic constitutive laws and ductile damage mechanisms would significantly broaden its application domain. To implement ductile fracture behavior, the TLSPH model would need to include plastic deformation mechanisms before failure occurs. This involves allowing particles to accumulate permanent strain when the stress exceeds a yield limit. Therefore, the total stretch between bonded particles can be decomposed into elastic and plastic components, allowing a modeling approach analogous to the damage framework introduced in the first part of this thesis. In addition, the relationship between plastic flow and material weakening should be defined so that failure happens more realistically under different loading conditions. This extended model can then be tested on standard problems like notched bars or specimens under impact to evaluate its ability to simulate necking, void growth, and ductile crack developmentfeatures that are essential for accurately modeling metals and other ductile materials.

Secondly, the proposed TLSPH framework focuses on modeling linear elastic solids and layered composite structures with orthotropic behavior. While this is sufficient for many engineering applications, it limits the ability to simulate materials with inherently nonlinear mechanical responses. A natural direction for future research is the integration of more advanced material models and crack propagation scenarios

into the existing particle-based scheme. In particular, hyperelastic materialssuch as rubbers, soft biological tissues, and elastomersexhibit large, recoverable deformations governed by nonlinear constitutive laws. Implementing hyperelasticity into the TLSPH context would involve updating the stress calculation procedure to derive the first Piola-Kirchhoff stress tensor from strain energy density functions, such as neo-Hookean or Mooney-Rivlin models. These models can better represent the mechanical response of materials subjected to extreme stretches, bending, or torsion. Furthermore, rate-dependent materials such as viscoelastic or viscoplastic solids could be introduced to simulate time-dependent deformation. This would allow the framework to address a wider range of problems, including polymer forming, soft tissue mechanics, and impact damping systems. In such cases, stress computation would rely not only on the instantaneous deformation state but also on the strain rate and time history. By integrating these more complex constitutive behaviors into the TLSPH framework, the model could be extended to simulate a much broader class of engineering and biological materials. This would significantly enhance its utility in applications involving soft structures, energy-absorbing components, and highly deformable media.

Another remaining challenge regarding to this research area is crack initiation and propagation in laminated composite structures. Due to the heterogeneous nature of compositesincluding fiber-matrix interfaces, ply orientations, and anisotropic stiffnessthe mechanisms of fracture are highly complex and depend on both local material behavior and global structural response. In composite laminates, cracks may initiate within plies (intra-laminar) or at ply interfaces (inter-laminar). The current TLSPH framework, which models each ply using discrete particles and orthotropic constitutive behavior, could be extended to incorporate bond-based damage and failure criteria across both intra- and inter-ply directions. This would require the definition of different critical stretch thresholds and damage evolution laws for particles within a ply versus those across adjacent plies. Another key consideration is the directional nature of failure. Fiber-dominated fracture mechanisms (e.g., fiber breakage or pullout) differ significantly from matrix-dominated ones (e.g., matrix cracking or delamination). Therefore, the failure behavior between bonded particles should account for fiber orientation, local stiffness contrast, and possibly mixed-mode loading effects. Embedding anisotropic damage criteria into the TLSPH formulation could help simulate these effects more realistically. Moreover, in many engineering environments, composite materials are exposed to fluctuating temperatures and moisture levels, which can significantly alter their mechanical performance and failure behavior.Thermal effects influence the stress distribution and deformation patterns in composites by inducing thermal strains, altering material stiffness,

and potentially causing interfacial delamination due to mismatched thermal expansion between plies. To model such behavior, the TLSPH formulation could be extended to include temperature as a field variable, solved using the transient heat conduction equation. The mechanical response of each particle would then depend not only on its deformation but also on its local temperature, accounting for thermal strain and temperature-dependent material properties. Similarly, the presence of moisture can lead to swelling, degradation of the matrix, reduction in interfacial bonding strength, and even stress corrosion cracking. Moisture ingress could be modeled as a diffusion process coupled with mechanical deformation, where the strain field would include hygroexpansion terms. Moisture content at each particle would evolve over time based on environmental exposure, material diffusivity, and boundary conditions. By incorporating these multiphysical phenomena into the TLSPH framework, it would be possible to simulate coupled responses such as thermally induced delamination, hygrothermal swelling, and degradation of mechanical performance over time.

In summary, the proposed TLSPH framework lays a solid foundation for the particle-based simulation of fracture and composite deformation; however, its full potential can be realized through systematic extensions in both physical modeling and computational strategy. Incorporating ductile and time-dependent material behavior, enabling fracture in complex composite systems, and accounting for environmental effects such as temperature and moisture would significantly broaden its range of applicability. These future developments would not only strengthen the frameworks predictive capabilities but also position it as a versatile tool for simulating real-world engineering systems with high fidelity. As computational power and parallelization techniques continue to evolve, the TLSPH approach stands to benefit from scalable implementations, enabling the simulation of increasingly large and complex structures with enhanced realism and reliability.

BIBLIOGRAPHY

Belytschko, T. & Black, T. (1999). Elastic crack growth in finite elements with minimal remeshing. *International Journal for Numerical Methods in Engineering*, *45*(5), 601–620.

Belytschko, T., Chen, H., Xu, J., & Zi, G. (2003). Dynamic crack propagation based on loss of hyperbolicity and a new discontinuous enrichment. *International Journal for Numerical Methods in Engineering*, *58*(12), 1873–1905.

Belytschko, T., Guo, Y., Kam Liu, W., & Ping Xiao, S. (2000). A unified stability analysis of meshless particle methods. *International Journal for Numerical Methods in Engineering*, *48*(9), 1359–1400.

Belytschko, T., Lu, Y., & Gu, L. (1995). Crack propagation by element-free galerkin methods. *Engineering Fracture Mechanics*, *51*(2), 295–315.

Belytschko, T., Lu, Y. Y., & Gu, L. (1994). Element-free galerkin methods. *International Journal for Numerical Methods in Engineering*, *37*(2), 229–256.

Belytschko, T. & Tabbara, M. (1996). Dynamic fracture using element-free galerkin methods. *International Journal for Numerical Methods in Engineering*, *39*(6), 923–938.

Benz, W. & Asphaug, E. (1995). Simulations of brittle solids using smooth particle hydrodynamics. *Computer Physics Communications*, *87*(1), 253–265. Particle Simulation Methods.

Bessa, M., Foster, J., Belytschko, T., & Liu, W. K. (2014). A meshfree unification: reproducing kernel peridynamics. *Computational Mechanics*, *53*, 1251–1264.

Borden, M. J., Verhoosel, C. V., Scott, M. A., Hughes, T. J., & Landis, C. M. (2012). A phase-field description of dynamic brittle fracture. *Computer Methods in Applied Mechanics and Engineering*, *217-220*, 77–95.

Braun, M. & Fernández-Sáez, J. (2014). A new 2d discrete model applied to dynamic crack propagation in brittle materials. *International Journal of Solids and Structures*, *51*(21), 3787–3797.

Chakraborty, S. & Shaw, A. (2013). A pseudo-spring based fracture model for sph simulation of impact dynamics. *International Journal of Impact Engineering*, *58*, 84–95.

Chen, J.-S., Wu, C.-T., Yoon, S., & You, Y. (2001). A stabilized conforming nodal integration for galerkin mesh-free methods. *International Journal for Numerical Methods in Engineering*, *50*(2), 435–466.

Cherniaev, A. & Telichev, I. (2015). Meso-scale modeling of hypervelocity impact damage in composite laminates. *Composites Part B: Engineering*, *74*, 95–103.

de Borst, R., Crisfield, M. A., Remmers, J. J. C., & Verhoosel, C. V. (2012). *Nonlinear Finite Element Analysis*, chapter 2, (pp. 31–111). John Wiley & Sons, Ltd.

Douillet-Grellier, T., Pramanik, R., Pan, K., Albaiz, A., Jones, B. D., & Williams, J. R. (2017). Development of stress boundary conditions in smoothed particle hydrodynamics (sph) for the modeling of solids deformation. *Computational Particle Mechanics*, *4*, 451–471.

Dyka, C. T., Randles, P. W., & Ingel, R. P. (1997). Stress points for tension instability in sph. *International Journal for Numerical Methods in Engineering*,

40(13), 2325–2341.

Ganzenmüller, G., Hiermaier, S., & May, M. (2015). On the similarity of meshless discretizations of peridynamics and smooth-particle hydrodynamics. *Computers & Structures*, *150*, 71–78.

Ganzenmüller, G. C. (2015). An hourglass control algorithm for lagrangian smooth particle hydrodynamics. *Computer Methods in Applied Mechanics and Engineering*, *286*, 87–106.

Ghajari, M., Iannucci, L., & Curtis, P. (2014). A peridynamic material model for the analysis of dynamic crack propagation in orthotropic media. *Computer Methods in Applied Mechanics and Engineering*, *276*, 431–452.

Ghorashi, S. S., Mohammadi, S., & Sabbagh-Yazdi, S.-R. (2011). Orthotropic enriched element free galerkin method for fracture analysis of composites. *Engineering Fracture Mechanics*, *78*(9), 1906–1927.

Giannaros, E., Kotzakolios, A., Kostopoulos, V., & Campoli, G. (2019). Hypervelocity impact response of cfrp laminates using smoothed particle hydrodynamics method: Implementation and validation. *International Journal of Impact Engineering*, *123*, 56–69.

Gingold, R. A. & Monaghan, J. J. (1977). Smoothed particle hydrodynamics: theory and application to non-spherical stars. *Monthly Notices of the Royal Astronomical Society*, *181*(3), 375–389.

Gu, Y., Wang, W., Zhang, L., & Feng, X.-Q. (2011). An enriched radial point interpolation method (e-rpim) for analysis of crack tip fields. *Engineering Fracture Mechanics*, *78*(1), 175–190.

Guo, S., Tian, X., & Tang, Y. (2024). Peridynamics-based model of composite lamina with progressive variations in mechanical properties. *Materials Today Communications*, *40*, 110158.

He, J. & Lei, J. (2019). A gpu-accelerated tlsph algorithm for 3d geometrical nonlinear structural analysis. *International Journal of Computational Methods*, *16*(07), 1850114.

He, J., Tofighi, N., Yildiz, M., Lei, J., & Suleman, A. (2017). A coupled wc-tl sph method for simulation of hydroelastic problems. *International Journal of Computational Fluid Dynamics*, *31*(3), 174–187.

He, L., Lu, G., Chen, D., Li, W., & Lu, C. (2017). Three-dimensional smoothed particle hydrodynamics simulation for injection molding flow of short fiber-reinforced polymer composites. *Modelling and Simulation in Materials Science and Engineering*, *25*(5), 055007.

Huntley, S., Rendall, T., Longana, M., Pozegic, T., Potter, K., & Hamerton, I. (2020). Validation of a smoothed particle hydrodynamics model for a highly aligned discontinuous fibre composites manufacturing process. *Composites Science and Technology*, *196*, 108152.

Islam, M. R. I. & Peng, C. (2019). A total lagrangian sph method for modelling damage and failure in solids. *International Journal of Mechanical Sciences*, *157*, 498–511.

Jun Lin, J., Naceur, H., Daniel, C., & Laksimi, A. (2015). Geometrically nonlinear analysis of two-dimensional structures using an improved smoothed particle hydrodynamics method. *Engineering Computations*, *32*, 779–805.

Kalthoff, J. & Winkler, S. (1988). Failure mode transition at high rates of shear loading. *DGM Informationsgesellschaft mbH, Impact Loading and Dynamic*

Behavior of Materials, *1*, 185–195.

Karamanli, A. (2016). Analysis of bending deflections of functionally graded beams by using different beam theories and symmetric smoothed particle hydrodynamics. *International Journal of Engineering Technologies IJET*, *2*(3), 105–117.

Karamanlı, A. (2017). Elastostatic analysis of two-directional functionally graded beams using various beam theories and symmetric smoothed particle hydrodynamics method. *Composite Structures*, *160*, 653–669.

Li, C., Ning, Y., & Liu, X. (2022). Discontinuous deformation analysis (dda) simulations of crack propagation, branching and coalescence in brittle materials under dynamic loading. *Theoretical and Applied Fracture Mechanics*, *122*, 103648.

Libersky, L. D., Petschek, A. G., Carney, T. C., Hipp, J. R., & Allahdadi, F. A. (1993). High strain lagrangian hydrodynamics: A three-dimensional sph code for dynamic material response. *Journal of Computational Physics*, *109*(1), 67–75.

Liew, K. M., Zhao, X., & Ferreira, A. J. (2011). A review of meshless methods for laminated and functionally graded plates and shells. *Composite Structures*, *93*(8).

Lin, J., Naceur, H., Coutellier, D., & Laksimi, A. (2014). Geometrically nonlinear analysis of thin-walled structures using efficient shell-based sph method. *Computational Materials Science*, *85*, 127–133.

Liu, G., Chen, X., & Reddy, J. (2002). Buckling of symmetrically laminated composite plates using the element-free galerkin method. *International Journal of Structural Stability and Dynamics*, *2*(03), 281–294.

Liu, M. & Liu, G. (2010). Smoothed particle hydrodynamics (sph): an overview and recent developments. *Archives of computational methods in engineering*, *17*, 25–76.

Liu, W. K., Jun, S., & Zhang, Y. F. (1995). Reproducing kernel particle methods. *International Journal for Numerical Methods in Fluids*, *20*(8-9), 1081–1106.

Lucy, L. B. (1977). A numerical approach to the testing of the fission hypothesis. *Astronomical Journal*, *82*, 1013–1024.

Madenci, E. & Oterkus, E. (2013). Peridynamic theory. In *Peridynamic theory and its applications*. Springer.

Mehrmashhadi, J., Chen, Z., Zhao, J., & Bobaru, F. (2019). A stochastically homogenized peridynamic model for intraply fracture in fiber-reinforced composites. *Composites Science and Technology*, *182*, 107770.

Moës, N. & Belytschko, T. (2002). Extended finite element method for cohesive crack growth. *Engineering Fracture Mechanics*, *69*(7), 813–833.

Ozbulut, M., Tofighi, N., Goren, O., & Yildiz, M. (2017). Investigation of Wave Characteristics in Oscillatory Motion of Partially Filled Rectangular Tanks. *Journal of Fluids Engineering*, *140*(4), 041204.

Pan, J.-H., Li, D., Luo, X.-B., & Zhu, W. (2022). An enriched improved complex variable element-free galerkin method for efficient fracture analysis of orthotropic materials. *Theoretical and Applied Fracture Mechanics*, *121*, 103488.

Partmann, K., Wieners, C., & Weinberg, K. (2023). Continuum-kinematics-based peridynamics and phase-field approximation of non-local dynamic fracture. *International Journal of Fracture*, *244*, 1–14.

Rabczuk, T. (2013). Computational methods for fracture in brittle and quasi-brittle solids: State-of-the-art review and future perspectives. *International Scholarly Research Notices*, *2013*(1), 849231.

Rabczuk, T. & Belytschko, T. (2004). Cracking particles: a simplified meshfree method for arbitrary evolving cracks. *International Journal for Numerical Methods in Engineering*, *61*(13), 2316–2343.

Rabczuk, T. & Belytschko, T. (2007). A three-dimensional large deformation meshfree method for arbitrary evolving cracks. *Computer Methods in Applied Mechanics and Engineering*, *196*(29), 2777–2799.

Rabczuk, T., Zi, G., Bordas, S., & Nguyen-Xuan, H. (2010). A simple and robust three-dimensional cracking-particle method without enrichment. *Computer Methods in Applied Mechanics and Engineering*, *199*(37), 2437–2455.

Rahimi, M. N., Koluksa, D., Yildiz, M., Ozbulut, M., & Kefal, A. (2022). A generalized hybrid smoothed particle hydrodynamics-peridynamics algorithm with a novel Lagrangian mapping for solution and failure analysis of fluid-structure interaction problems. *Computer Methods in Applied Mechanics and Engineering*, *389*, 114370.

Rahimi, M. N. & Moutsanidis, G. (2022). A smoothed particle hydrodynamics approach for phase field modeling of brittle fracture. *Computer Methods in Applied Mechanics and Engineering*, *398*, 115191.

Rahmat, A. & Yildiz, M. (2018). A multiphase isph method for simulation of droplet coalescence and electro-coalescence. *International Journal of Multiphase Flow*, *105*, 32–44.

Ramalho, L., Belinha, J., & Campilho, R. (2019). The numerical simulation of crack propagation using radial point interpolation meshless methods. *Engineering Analysis with Boundary Elements*, *109*, 187–198.

Randles, P. & Libersky, L. (1996). Smoothed particle hydrodynamics: Some recent improvements and applications. *Computer Methods in Applied Mechanics and Engineering*, *139*(1), 375–408.

Ravi-Chandar, K. (1998). Dynamic fracture of nominally brittle materials. *International Journal of fracture*, *90*, 83–102.

Raymond, S., Lemiale, V., Ibrahim, R., & Lau, R. (2014). A meshfree study of the kalthoffwinkler experiment in 3d at room and low temperatures under dynamic loading using viscoplastic modelling. *Engineering Analysis with Boundary Elements*, *42*, 20–25. Advances on Meshfree and other Mesh reduction methods.

Reddy, J. N. (2004). *Mechanics of Laminated Composite Plates and Shells: Theory and Analysis* (Second ed.). Boca Raton, FL: CRC Press.

Ren, H., Zhuang, X., Anitescu, C., & Rabczuk, T. (2019). An explicit phase field method for brittle dynamic fracture. *Computers & Structures*, *217*, 45–56.

Ren, H., Zhuang, X., & Rabczuk, T. (2017). Dual-horizon peridynamics: A stable solution to varying horizons. *Computer Methods in Applied Mechanics and Engineering*, *318*, 762–782.

Rodrigues, D., Belinha, J., Dinis, L., & Jorge, R. N. (2021). The bending behaviour of antisymmetric cross-ply laminates using high-order shear deformation theories and a radial point interpolation method. In *Structures*, volume 32, (pp. 1589–1603). Elsevier.

Rodrigues, D., Belinha, J., & Natal Jorge, R. (2021). The radial point interpolation method in the bending analysis of symmetric laminates using hsdts. *Journal*

of Computational Applied Mechanics, *52*(4), 682–716.

Saitta, S., Luciano, R., Vescovini, R., Fantuzzi, N., & Fabbrocino, F. (2022). Free vibrations and buckling analysis of cross-ply composite nanoplates by means of a mesh free radial point interpolation method. *Composite Structures*, *298*, 115989.

Shadloo, M., Zainali, A., & Yildiz, M. (2013). Simulation of single mode rayleigh–taylor instability by sph method. *Computational Mechanics*, *51*, 699–715.

Shadloo, M. S., Zainali, A., Sadek, S. H., & Yildiz, M. (2011). Improved incompressible smoothed particle hydrodynamics method for simulating flow around bluff bodies. *Computer Methods in Applied Mechanics and Engineering*, *200*(9), 1008–1020.

Shepard, D. (1968). A two-dimensional interpolation function for irregularly-spaced data. In *Proceedings of the 1968 23rd ACM National Conference*, ACM '68, (pp. 517524)., New York, NY, USA. Association for Computing Machinery.

Silling, S. A. (2000). Reformulation of elasticity theory for discontinuities and long-range forces. *Journal of the Mechanics and Physics of Solids*, *48*, 175–209.

Song, J.-H., Areias, P. M. A., & Belytschko, T. (2006). A method for dynamic crack and shear band propagation with phantom nodes. *International Journal for Numerical Methods in Engineering*, *67*(6), 868–893.

Sukumar, N., Moës, N., Moran, B., & Belytschko, T. (2000). Extended finite element method for three-dimensional crack modelling. *International Journal for Numerical Methods in Engineering*, *48*(11), 1549–1570.

Swegle, J., Hicks, D., & Attaway, S. (1995). Smoothed particle hydrodynamics stability analysis. *Journal of Computational Physics*, *116*(1), 123–134.

Vignjevic, R., Vuyst, T., & orevi, N. (2024). Modelling of damage in composites using smooth particle hydrodynamics method. *Journal of the Serbian Society for Computational Mechanics*, *18*, 45–66.

Wang, J. & Liu, G. (2002). A point interpolation meshless method based on radial basis functions. *International Journal for Numerical Methods in Engineering*, *54*(11), 1623–1648.

Wiragunarsa, I. M., Zuhal, L. R., Dirgantara, T., & Putra, I. S. (2021). A particle interaction-based crack model using an improved smoothed particle hydrodynamics for fatigue crack growth simulations. *International Journal of Fracture*, *229*(2), 229–244.

Xu, D., Liu, Z., Liu, X., Zeng, Q., & Zhuang, Z. (2014). Modeling of dynamic crack branching by enhanced extended finite element method. *Computational Mechanics*, *54*, 489–502.

Zhang, A.-M., Ming, F., & Cao, X. (2014). Total lagrangian particle method for the large deformation analyses of solids and curved shells. *Acta Mechanica*, *225*, 253275.

Zhou, T. & Song, Y. (2019). Three-dimensional nonlinear bending analysis of fg-cnts reinforced composite plates using the element-free galerkin method based on the sr decomposition theorem. *Composite Structures*, *207*, 519–530.

Zhou, X., Wang, Y., & Qian, Q. (2016). Numerical simulation of crack curving and branching in brittle materials under dynamic loads using the extended non-ordinary state-based peridynamics. *European Journal of Mechanics - A/Solids*, *60*, 277–299.

Zhou, X., Yao, W.-W., & Berto, F. (2021). Smoothed peridynamics for the ex-

tremely large deformation and cracking problems: Unification of peridynamics and smoothed particle hydrodynamics. *Fatigue & Fracture of Engineering Materials & Structures*, *44*(9), 2444–2461.

Zhuang, X., Cai, Y., & Augarde, C. (2014). A meshless sub-region radial point interpolation method for accurate calculation of crack tip fields. *Theoretical and Applied Fracture Mechanics*, *69*, 118–125.

APPENDIX A

This section details the derivation of the SPH interpolation scheme. To begin with, the position vector of particle **i** is $\mathbf{r_i} = \mathbf{x_i^k}\hat{\mathbf{e}}_k$ where $\mathbf{x_i^k}$ is the component of the position vector with k = 1,2,3 and $\hat{\mathbf{e}}_k$ is the base vector. Thus, the distance vector $\mathbf{r_{ij}}$ between particle **i** and particle **j** is denoted as:

$$\begin{aligned} \mathbf{r_{ij}} &= \mathbf{r_i} - \mathbf{r_j} = (\mathbf{x_i^k} - \mathbf{x_j^k})\hat{\mathbf{e}}_k = \mathbf{r_{ij}^k}\hat{\mathbf{e}}_k, \\ \mathbf{r_{ji}} &= \mathbf{r_j} - \mathbf{r_i} = (\mathbf{x_j^k} - \mathbf{x_i^k})\hat{\mathbf{e}}_k = \mathbf{r_{ji}^k}\hat{\mathbf{e}}_k. \end{aligned} \tag{A.1}$$

Please note that the magnitude of $\mathbf{r_{ij}}$ is $r_{\mathbf{ij}}$. To derive the main SPH interpolation functions, one can start with the Dirac delta function $\delta(x - x_0)$. To be able to analyze this function, the unit step (Heaviside) function H(x) which has a jump at x = 0 can be introduced. This function takes the value of 0 for $x < 0$ and value of 1 for $x \geq 0$. If this function is shifted to the right by a positive number "a", it is written as H(x-a). Therefore, the integral of a continious function f(x) between the boundaries a and b, $a \leq x \leq b$, can be written as:

$$\int_a^b f(x)dx = \int_{-\infty}^{+\infty} f(x)[H(x-a) - H(x-b)]dx. \tag{A.2}$$

If the integral boundaries are changed as $a = x_0 - \frac{\varepsilon}{2}$ and $b = x_0 + \frac{\varepsilon}{2}$ and mean-value theorem is applied, a window function $\overline{W}(x - x_0, \varepsilon) = \frac{H((x-x_0)+\varepsilon/2) - H((x-x_0)-\varepsilon/2)}{\varepsilon}$ appears. If the ε is small enough, the function becomes an impulse function, in which x_0 is the center position of the impulse. The integral in Equation A.2 becomes:

$$\int_{-\infty}^{+\infty} f(x)\frac{\overline{W}(x - x_0, \varepsilon)}{\varepsilon}dx = f(\xi), \tag{A.3}$$

where ξ is a number such that $x_0 - \frac{\varepsilon}{2} \leq \xi \leq x_0 + \frac{\varepsilon}{2}$. Taking the limit of Equation A.3 as $\varepsilon \to 0$, results in two functions: Dirac delta function $\delta(x - x_0)$, i.e., limit of the window function $\overline{W}$, and $\lim_{\varepsilon \to 0} f(\xi) = f(x_0)$. After the limit operation, Equation A.3 becomes:

$$\int_{-\infty}^{+\infty} f(x)\delta(x - x_0)dx = f(x_0) \tag{A.4}$$

Since the integral of the Dirac delta function between $-\infty$ and $+\infty$ equals to 1 and $\delta(x - x_0) = \delta(x_0 - x)$, Dirac delta function is an even function, meaning that 3D Dirac delta function in Cartesian coordinates, $\delta^3(|\mathbf{r} - \mathbf{r}_0|) = \delta(x^1 - x_0^1)\delta(x^2 - x_0^2)\delta(x^3 - x_0^3)$, is also an even function. Thus, the integral of δ^3 through the space Ω (differential volume) is equal to 1. Finally, the formulation Equation A.4 can be denoted as:

$$\int_\Omega f(\mathbf{r})\delta^3(|\mathbf{r} - \mathbf{r}_0|)d^3\mathbf{r} = f(\mathbf{r}_0). \tag{A.5}$$

If the function δ^3 is replaced by a normalized distribution function, the SPH interpolation is obtained. This so-called distribution function is referred as Kernel function in SPH. For δ^3 to be replaced by a Kernel function, several conditions must be met;

- Normalization condition

$$\int_\Omega W(|\mathbf{r}-\mathbf{r}_0|,h)d^3\mathbf{r}=1. \tag{A.6}$$

- Dirac delta function property

$$\lim_{h\to 0} W(|\mathbf{r}-\mathbf{r}_0|,h)=\delta^3(|\mathbf{r}-\mathbf{r}_0|,h). \tag{A.7}$$

- Compact support property

$$W(|\mathbf{r}-\mathbf{r}_0|,h)=0 \quad \text{when} \quad |\mathbf{r}-\mathbf{r}_0|>\kappa h. \tag{A.8}$$

κh is a radius that defines the domain after which the kernel function is zero and h is the smoothing length. If above criteria are satisfied Dirac delta function in Equation A.5 can be replaced with a kernel function. Thus, the SPH kernel approximation ($\langle\rangle$) of a function can be expressed as:

$$f(\mathbf{r_i}) \approx \langle f(\mathbf{r_i})\rangle = \int_\Omega f(\mathbf{r_j})W(\mathbf{r_{ij}},h)d^3\mathbf{r_j}, \tag{A.9}$$

and the gradient of a function can be written as:

$$\frac{\partial f^k(\mathbf{r_i})}{\partial x^l_\mathbf{i}} \approx \left\langle \frac{\partial f^k(\mathbf{r_i})}{\partial x^l_\mathbf{i}} \right\rangle = \int_\Omega \frac{\partial f^k(\mathbf{r_j})}{\partial x^l_\mathbf{j}} W(\mathbf{r_{ij}},h)d^3\mathbf{r_j}. \tag{A.10}$$

Applying the product rule to the right hand side of Equation A.10:

$$\frac{\partial f^k(\mathbf{r_i})}{\partial x^l_\mathbf{i}} \approx \int_\Omega f^k(\mathbf{r_j}) \frac{\partial W(\mathbf{r_{ij}},h)}{\partial x^l_\mathbf{i}} d^3\mathbf{r_j}. \tag{A.11}$$

In above equation, $d^3\mathbf{r_j}$ is volume of the particle $\mathbf{j}$ and equals to m_j/ρ_j in which m is the mass of a particle. Thus, Equation A.9 and Equation A.11 can be discretized

as:

$$f(\mathbf{r_i}) = \sum_{\mathbf{j}=1}^{N} \frac{m_\mathbf{j}}{\rho_\mathbf{j}} f(\mathbf{r_j}) W(r_\mathbf{ij}, h), \tag{A.12}$$

$$\frac{\partial f(\mathbf{r_i})}{\partial x_\mathbf{i}^\mathbf{k}} = \sum_{\mathbf{j}=1}^{N} \frac{m_\mathbf{j}}{\rho_\mathbf{j}} f(\mathbf{r_j}) \frac{\partial W(r_\mathbf{ij}, h)}{\partial x_\mathbf{i}^\mathbf{k}} \tag{A.13}$$

To incorporate the density of particle $\mathbf{i}$, one can start with below equation via product rule of differentiation:

$$\frac{\partial(\rho_\mathbf{i} f(\mathbf{r_i}))}{\partial x_\mathbf{i}^k} = \rho_\mathbf{i} \frac{\partial f(\mathbf{r_i})}{\partial x_\mathbf{i}^k} + f(\mathbf{r_i}) \frac{\partial \rho_\mathbf{i}}{\partial x_\mathbf{i}^k}. \tag{A.14}$$

Thus the first term on the right hand side of the equation is:

$$\rho_\mathbf{i} \frac{\partial f(\mathbf{r_i})}{\partial x_\mathbf{i}^k} = \frac{\partial(\rho_\mathbf{i} f(\mathbf{r_i}))}{\partial x_\mathbf{i}^k} - f(\mathbf{r_i}) \frac{\partial \rho_\mathbf{i}}{\partial x_\mathbf{i}^k}. \tag{A.15}$$

Using the Equation A.12 and Equation A.13:

$$\frac{\partial f(\mathbf{r_i})}{\partial x_\mathbf{i}^\mathbf{k}} = \sum_{\mathbf{j}=1}^{N} \frac{m_\mathbf{j}}{\rho_\mathbf{i}} (f(\mathbf{r_j}) - f(\mathbf{r_i})) \frac{\partial W(r_\mathbf{ij}, h)}{\partial x_\mathbf{i}^\mathbf{k}}. \tag{A.16}$$

Equation A.16 is one way to obtain the gradient of a scalar-valued function. For the divergence of a vector-valued function, we can rewrite it as below:

$$\frac{\partial f^k(\mathbf{r_i})}{\partial x_\mathbf{i}^\mathbf{k}} = \sum_{\mathbf{j}=1}^{N} \frac{m_\mathbf{j}}{\rho_\mathbf{i}} \left(f^k(\mathbf{r_j}) - f^k(\mathbf{r_i}) \right) \frac{\partial W(r_\mathbf{ij}, h)}{\partial x_\mathbf{i}^\mathbf{k}}. \tag{A.17}$$

To obtain another way for differentiation of functions, one can start with product rule of differentiation of below equation as:

$$\frac{\partial}{\partial x_\mathbf{i}^\mathbf{m}} \left(\frac{f(\mathbf{r_i})}{\rho_\mathbf{i}} \right) = \frac{1}{\rho_\mathbf{i}} \frac{\partial f(\mathbf{r_i})}{\partial x_\mathbf{i}^\mathbf{m}} - \frac{f(\mathbf{r_i})}{\rho_\mathbf{i}^2} \frac{\partial \rho_\mathbf{i}}{\partial x_\mathbf{i}^\mathbf{m}}, \tag{A.18}$$

$$\frac{1}{\rho_\mathbf{i}} \frac{\partial f(\mathbf{r_i})}{\partial x_\mathbf{i}^\mathbf{m}} = \frac{\partial}{\partial x_\mathbf{i}^\mathbf{m}} \left(\frac{f(\mathbf{r_i})}{\rho_\mathbf{i}} \right) + \frac{f(\mathbf{r_i})}{\rho_\mathbf{i}^2} \frac{\partial \rho_\mathbf{i}}{\partial x_\mathbf{i}^\mathbf{m}}. \tag{A.19}$$

Using the Equation A.12 and Equation A.13:

$$\frac{\partial}{\partial x_\mathbf{i}^\mathbf{m}} \left(\frac{f(\mathbf{r_i})}{\rho_\mathbf{i}} \right) = \sum_{\mathbf{j}=1}^{N} \frac{m_\mathbf{j}}{\rho_\mathbf{j}} \frac{f(\mathbf{r_j}) \partial W(r_\mathbf{ij}, h)}{\rho_\mathbf{j} \partial x_\mathbf{i}^\mathbf{m}}, \tag{A.20}$$

$$\frac{f(\mathbf{r_i}) \partial \rho_\mathbf{i}}{\rho_\mathbf{i}^2 \partial x_\mathbf{i}^\mathbf{m}} = \frac{f(\mathbf{r_i})}{\rho_\mathbf{i}^2} \sum_{\mathbf{j}=1}^{N} \frac{m_\mathbf{j}}{\rho_\mathbf{j}} \frac{\partial W(r_\mathbf{ij}, h)}{\partial x_\mathbf{i}^\mathbf{m}}. \tag{A.21}$$

Combining above equations lead to second way of obtaining the gradient of a scalar-valued function as:

$$\frac{1}{\rho_{\mathbf{i}}}\frac{\partial f(\mathbf{r_i})}{\partial x_{\mathbf{i}}^{\mathbf{m}}} = \sum_{\mathbf{j}=1}^{N} m_{\mathbf{j}} \left(\frac{f(\mathbf{r_i})}{\rho_{\mathbf{i}}^2} + \frac{f(\mathbf{r_j})}{\rho_{\mathbf{j}}^2} \right) \frac{\partial W(r_{\mathbf{ij}}, h)}{\partial x_{\mathbf{i}}^{\mathbf{m}}} \tag{A.22}$$

Finally, the second way of gradient and divergence of a vector-valued function can be expressed as:

$$\frac{1}{\rho_{\mathbf{i}}}\frac{\partial f^{\mathbf{k}}(\mathbf{r_i})}{\partial x_{\mathbf{i}}^{\mathbf{l}}} = \sum_{\mathbf{j}=1}^{N} m_{\mathbf{j}} \left(\frac{f^{\mathbf{k}}(\mathbf{r_i})}{\rho_{\mathbf{i}}^2} + \frac{f^{\mathbf{k}}(\mathbf{r_j})}{\rho_{\mathbf{j}}^2} \right) \frac{\partial W(r_{\mathbf{ij}}, h)}{\partial x_{\mathbf{i}}^{\mathbf{l}}} \tag{A.23}$$

$$\frac{1}{\rho_{\mathbf{i}}}\frac{\partial f^{\mathbf{k}}(\mathbf{r_i})}{\partial x_{\mathbf{i}}^{\mathbf{k}}} = \sum_{\mathbf{j}=1}^{N} m_{\mathbf{j}} \left(\frac{f^{\mathbf{k}}(\mathbf{r_i})}{\rho_{\mathbf{i}}^2} + \frac{f^{\mathbf{k}}(\mathbf{r_j})}{\rho_{\mathbf{j}}^2} \right) \frac{\partial W(r_{\mathbf{ij}}, h)}{\partial x_{\mathbf{i}}^{\mathbf{k}}} \tag{A.24}$$